

# Boundary modulation effects on MHD instabilities in heliotrons

N. Nakajima<sup>1</sup>, S.R. Hudson<sup>2</sup>, C.C. Hegna<sup>3</sup> and Y. Nakamura<sup>4</sup>

<sup>1</sup> National Institute for Fusion Science, Oroshi-cho 322-6, Toki 509-5292, Japan

<sup>2</sup> Princeton Plasma Physics Laboratory, PO Box 451, Princeton, NJ 08543, USA

<sup>3</sup> Department of Engineering Physics, University of Wisconsin–Madison, WI 53706, USA

<sup>4</sup> Graduate School of Energy Science, Kyoto University, Uji, Kyoto 611-0011, Japan

E-mail: [nakajima@nifs.ac.jp](mailto:nakajima@nifs.ac.jp)

Received 24 January 2005, accepted for publication 18 November 2005

Published 4 January 2006

Online at [stacks.iop.org/NF/46/177](http://stacks.iop.org/NF/46/177)

## Abstract

In three-dimensional configurations, the confinement region is surrounded by the stochastic magnetic field lines related to magnetic islands or separatrix, leading to the fact that the plasma–vacuum boundary is not so definite compared with tokamaks that the various modulations of the plasma–vacuum boundary will be induced around the stochastic region by synergetic effects between a transport around the stochastic region and a large Shafranov shift of the whole plasma, in especially high- $\beta$  operations. To examine such modulation effects of the plasma boundary on MHD instabilities, high- $\beta$  plasmas allowing a large Shafranov shift or a large Pfirsch–Schlüter current are considered in the inward-shifted LHD configurations with the vacuum magnetic axis  $R_{ax}$  of 3.6 m, for which previous theoretical analyses based on fixed MHD equilibria indicate that pressure-driven modes are significantly more unstable compared with experimental observations. The concept of the averaged flux surfaces allowing a movement of the equilibrium plasma into the stochastic region is introduced, which induces a boundary modulation and, at the same time, reduces the discrepancy on MHD equilibria between the experimentally obtained and theoretically considered. As a result, it is shown that the boundary modulation, namely, the whole plasma outward-shift due to a large Pfirsch–Schlüter current has significant stabilizing effects on ideal MHD instabilities, leading to partially resolving the discrepancy on MHD stability between experimental results and theoretical analyses.

**PACS numbers:** 52.55.Hc, 52.55.Tn

(Some figures in this article are in colour only in the electronic version)

## 1. Introduction

The structure of the ideal MHD spectrum is completely determined by the MHD equilibrium and the mass density profile. In order to analyse the experimental data on the MHD stability or energetic ion-driven modes like toroidicity-induced shear Alfvén eigenmodes (TAE) and helicity-induced shear Alfvén eigenmodes (HAE), the net toroidal current profile or the rotational transform profile, the pressure profile and the boundary condition must be estimated from the experimental results as accurately as possible, because the MHD equilibrium is determined by these three conditions. On the other hand, the extension of the MHD model to include micro multi-scales, like ion and electron diamagnetic frequencies and ion and electron skin depths, namely as an initiative to an extended MHD, has been started. In this type of extension, to make a precise equilibrium is one of the key points, in order to evaluate the difference between the MHD model and the extended MHD model, and to show the usefulness of the extended MHD

model for analyses of the experimental data. In the case of the three-dimensional magnetic configurations, however, the plasma boundary is not so definite compared with tokamaks due to the stochastic magnetic field surrounding the nested flux surfaces. The transport in such a stochastic magnetic field (change in the temperature and the density) and the internal plasma current like a Pfirsch–Schlüter current (change in the magnetic field) simultaneously interact, and the MHD equilibrium will be determined as a result of their synergetic effects. In other words, there is a possibility that the boundary will be modulated from the simple fixed boundary determined by the clear vacuum last close flux surface. In order to examine such the modulation effects of the plasma–vacuum boundary on MHD instabilities, high- $\beta$  plasmas allowing a large Shafranov shift or a large Pfirsch–Schlüter current are considered in the inward-shifted LHD configurations.

Recently, high- $\beta$  plasmas with  $\beta \gtrsim 3\%$ , where  $\beta$  is the ratio of the averaged kinetic pressure to the averaged magnetic pressure, have been established in the inward-shifted LHD

configurations with the vacuum magnetic axis  $R_{ax}$  of 3.6 m [1, 2], for which previous theoretical ideal MHD stability analyses based on fixed boundary equilibria have shown that pressure-driven modes are significantly more unstable compared with experimental observations [3]. There may be two types of thought to remove this discrepancy between theoretical and experimental results. One is to show that the nonlinear saturation level of the linear modes may be too low to influence the confinement performance [4] and/or to show that some two-fluid or kinetic effects added to the MHD model may have strong stabilizing effects. The other is to reconsider the MHD equilibria themselves used in the linear and nonlinear stability analyses, because the stability properties of the linearized ideal MHD modes are completely determined by the used MHD equilibria. It should be noted that, in previous theoretical considerations, the MHD equilibria are mainly created under the fixed boundary corresponding to a *clear* last closed flux surface (LCFS) of the vacuum magnetic field [3, 5], and that, even in the free boundary equilibrium calculations, an artificial material limiter is introduced to settle the plasma boundary on the clear LCFS of the vacuum magnetic field at the outboard of the horizontally elongated poloidal cross section, on which the plasma pressure is assumed to vanish [4, 6]. In these analyses, the resultant MHD equilibria are strongly unstable against the pressure-driven ideal MHD modes in the inward-shifted LHD configurations.

These theoretical methods to determine the MHD equilibria are based on the conjecture that the plasma does not expand beyond the clear LCFS of the vacuum field so much. Generally speaking, the clear LCFS of the vacuum magnetic field is usually surrounded by unclear flux surfaces or stochastic magnetic field lines in the three-dimensional magnetic configurations. Thus, the above conjecture might be correct, when the magnetic field lines in such peripheral stochastic region have a quite short connection length or those field lines are short open field lines compared with the parallel mean free path. However, there is a case where the magnetic field lines in the peripheral stochastic region have a fairly long connection length compared with the parallel mean free path and a definite rotational transform, which might be the case in LHD. In such a case, when the electron thermal conductivity is not so large in the peripheral stochastic region, the region with stochastic magnetic field might be considered to potentially have the confinement properties. Indeed, there are standard experimental observations that (1) the electron temperature gradient extends beyond the vacuum LCFS [7], (2) the electron density profile is significantly hollow and expands beyond the vacuum LCFS [8] and (3) from the low- $\beta$  or with increasing  $\beta$ , magnetic perturbations with the resonant rational surfaces near or beyond the vacuum LCFS are observed by the magnetic probes [9–11]. The first two experimental results indicate that the stochastic magnetic field surrounding nested flux surfaces holds confinement properties or pressure gradient and plasma expands beyond the vacuum LCFS and the third observation denotes that such a pressure gradient in the stochastic region is large enough to drive the MHD instabilities. Since the magnitude of the temperature in the stochastic region is small, it might be considered that the low temperature and high density plasma exist in the stochastic region, leading to the short parallel mean free path to the magnetic field.

In the three-dimensional configurations, it is quite difficult to determine the plasma–vacuum boundary useful for MHD stability analyses, because the experimentally observed confinement properties in the stochastic magnetic field region are mainly determined by the transport process there. This situation is completely different from tokamaks with clear flux surfaces and separatrix. On the other hand, in heliotron configurations like LHD, the Shafranov shift is fairly large, namely, a large Pfirsch–Schlüter current (internal plasma current) flows in equilibrium, which changes the plasma–vacuum boundary through the change in the magnetic field in both the plasma and the vacuum regions. Especially, the pressure profile with a steep gradient near the plasma boundary, which is suggested from experimental observations, induces a significant Pfirsch–Schlüter current near the plasma boundary, leading to a strong modification of the magnetic field in the vacuum stochastic region. In the experiments, of course, the MHD equilibrium strongly links the transport, and both should be determined simultaneously. In order to take into account the above standard experimental observations [7–11], from two aspects, namely transport and equilibrium, a new conjecture is introduced that averaged flux surfaces with confinement properties are created in the region with stochastic magnetic field. The averaged flux surfaces are defined as a confinement region with a long connection length compared with the parallel mean free path, a definite rotational transform and a small electron thermal conductivity. The averaged flux surfaces should be considered to be the result of both the transport process and change in the magnetic field in the stochastic region. Thus, it is natural to consider that a movement of the equilibrium plasma by a large internal plasma current into a region with averaged flux surfaces is allowable and that a boundary modulation induced by the plasma free motion might bring MHD equilibria into a state with a lower free energy compared with that under the fixed boundary. Indeed, the optimization of the three-dimensional magnetic configurations has been done by controlling the plasma–vacuum boundary shape [12].

In this work, analyses on MHD equilibria and stability in the inward-shifted LHD configurations are reconsidered from the aspect of the boundary modulation based on the conjecture that averaged flux surfaces are created in the stochastic vacuum magnetic field region. To consider free boundary MHD equilibria allowing the boundary modulation leads to reduction of the discrepancy on MHD equilibria between the experimentally obtained and the theoretically used, judging from the experimental observations [7–11]. As a result, it is shown that the boundary modulation due to a free motion of equilibrium plasma into the stochastic region with the averaged flux surfaces, namely a whole plasma outward shift in the major radius direction, has significant stabilizing effects on the linearized ideal MHD stability with increasing  $\beta$ , which may also lead to a partial removal of discrepancy on MHD stability between experimental results and the previous theoretical results based on the MHD equilibria with a fixed boundary.

A comparison between experimental observation of the magnetic signal and the standard MHD stability analyses based on the fixed boundary MHD equilibria are given in section 2, in order to clarify the relation of the MHD stability

between experimental results and the standard theoretical consideration. In section 3, several MHD equilibria with different plasma–vacuum boundary are selected based on the concept of the averaged flux surfaces, taking into account the properties of the vacuum magnetic field in the inward-shifted LHD configurations. The reason why several plasma–vacuum boundaries are selected comes from the fact that the systematic method of determining the plasma–vacuum boundary is not found to take into account the transport in the stochastic region. The properties of the Fourier modes of the plasma boundary in selected MHD equilibria are discussed in section 4, where it is shown that the change of the spectrum by the Shafranov shift of the whole plasma or by the internal plasma current is similar to that by the outward-shift of the vacuum magnetic axis due to the external coil current, and that the most significant change comes from the poloidally symmetric components with  $(m, n) = (0, \neq 0)$ , where  $m$  and  $n$  are the poloidal and toroidal Fourier mode numbers, respectively. For the MHD equilibrium calculations, vmec code [13] is used, where the pressure profile and the net toroidal current condition are determined on the basis of the experimental observations. The linearized ideal MHD stability analyses are performed in section 5, where cas3d3 code [14], based on the variational or energy principle, is used for low- $n$  incompressible or compressible perturbations under the fixed or free boundary condition. The dependence of the growth rates on both the boundary condition of MHD equilibria and the  $\beta$  values is clearly shown, which means that the boundary modulation, namely, a whole plasma outward-shift by a large Pfirsch–Schlüter current has significant stabilizing effects on linearized ideal MHD instabilities in the inward-shifted LHD configurations. Section 6 is devoted to the summary and discussions.

## 2. Experimental results and standard MHD stability analyses

In order to clarify the relation between experimental results and theoretical consideration in the inward-shifted LHD configurations, magnetic perturbations observed by the magnetic probes and the standard ideal MHD stability analyses of the incompressible perturbations for the fixed boundary MHD equilibria are compared for two types of the inward-shifted LHD configurations. One of them is the inward-shifted configuration with  $\gamma_c = 1.254$  and the other is that with  $\gamma_c = 1.220$ , where  $\gamma_c$  is the coil inverse aspect ratio defined by  $\gamma_c = (M/L)(a_c/R)$ .  $M$  and  $L$  are the toroidal field period and coil polarity of the helical coils, respectively (for LHD,  $M = 10$  and  $L = 2$ ).  $a_c$  and  $R$  are the minor and major radii of the helical coils, respectively (for LHD,  $R = 3.9$  m). Thus,  $\gamma_c = 1.254$  ( $\gamma_c = 1.220$ ) means  $a_c = 0.978$  m ( $a_c = 0.952$  m). This configuration change can be brought about using the fact that the helical coil of LHD consists of the three layers with independent power supply. The inward-shifted configuration with  $\gamma_c = 1.254$  has been extensively used for high- $\beta$  operations, in which high  $\beta$  plasma with  $\langle\beta_{\text{dia}}\rangle = 3.2\%$  has been achieved [1], where  $\langle\beta_{\text{dia}}\rangle$  is the diamagnetic beta value defined as  $4\mu_0/3 \cdot W_{\text{dia}}/(2B_{\text{av}}V_p)$  [10]. The notation of  $W_{\text{dia}}$  is the diamagnetic energy and  $B_{\text{av}}$  and  $V_p$  are the averaged vacuum toroidal magnetic fields

inside the plasma boundary and the corresponding plasma volume, respectively, and  $\mu_0$  is the permeability in the vacuum. The inward-shifted configuration with  $\gamma_c = 1.220$  has been pursued in order to achieve higher  $\beta$  plasma than that in the configuration with  $\gamma_c = 1.254$ , and finally  $\langle\beta_{\text{dia}}\rangle = 4.1\%$  has been achieved [2]. The inward-shifted configuration with  $\gamma_c = 1.220$  is considered to have a better deposition profile of the energetic ions due to NBI than that in the inward-shifted configuration with  $\gamma_c = 1.254$ , because a higher aspect ratio (lower  $\gamma_c$ ) is considered to be favourable for recovering the helical symmetry in the inward-shifted LHD configuration.

Two standard examples of the magnetic signals observed by the magnetic probes are shown in figure 1 for inward-shifted LHD configuration with  $\gamma_c = 1.254$ . The magnetic probes are settled just in front of the helical coils and in the toroidal direction, and so the range of the decomposed Fourier modes is  $m = 0\text{--}3$  and  $n = 0\text{--}5$ , where  $m$  and  $n$  are the poloidal and toroidal Fourier modes, respectively.

Typically in the range with  $\langle\beta_{\text{dia}}\rangle < 2\%$ , significant  $n/m = 1/2$  activities are observed, as is shown in shot number 44238. Since, as is understood from the discussion in the next section, the vacuum rotational transform at clear LCFS is around  $t_v \sim 1.48$ , it is found that perturbations with the Fourier modes resonating at the plasma periphery ( $n/m = 1/1$ ) or near the plasma edge ( $n/m = 3/2$ ) are strongly excited almost independent of  $\langle\beta_{\text{dia}}\rangle$ . In table 1,  $\langle\beta_{\text{dia}}\rangle$ -dependence of experimentally observed Fourier modes is summarized in such MHD equilibria that the currentless approximation is suitable ( $I_p/B_T \sim 10$  kA T $^{-1}$  where  $I_p$  and  $B_T$  are the observed net toroidal current and the vacuum toroidal fields, respectively). Note that all the Fourier modes indicated in table 1 are not necessarily observed in one shot. Which modes are observed depends on the experimental conditions as is understood from figure 1.

From table 1, it is understood that (1) although instabilities with  $n/m = 1/2$  resonating in the plasma core region are observed in the relatively low  $\langle\beta_{\text{dia}}\rangle$ , they disappear as  $\langle\beta_{\text{dia}}\rangle$  increases beyond 2%, (2) the higher harmonics are simultaneously excited at the plasma periphery with  $t = 1$  almost independent of  $\langle\beta_{\text{dia}}\rangle$  (in high density operations, almost only  $n/m = 1/1$  modes are observed) and (3) instabilities resonating near the plasma boundary ( $n/m = 4/3, 3/2$ ) are always excited almost independent of  $\beta$  values. Note that the range of the Fourier modes analysed from the magnetic probe data is limited especially for the poloidal mode number  $m$  (for the toroidal mode number, all mode families in LHD with  $M = 10$  are covered;  $n_f = 0 \sim 5$ ).

The standard examples of the magnetic signals observed by the magnetic probes are shown in figure 2 for inward-shifted LHD configuration with  $\gamma_c = 1.220$ . In this configuration, the vacuum clear LCFS exists around  $t_v \sim 1.78$  as is discussed in the next section. Comparing with shot number 46346, the plasma in shot number 46337 corresponds to a relatively high density case. It is understood that the Fourier modes resonating nearer the plasma edge, for example  $n/m = 2/1, 5/2$ , are significantly excited as the density increases. Note that the resonant rational surfaces of these two modes exist outside the vacuum LCFS (see next section).

$\langle\beta_{\text{dia}}\rangle$ -dependence of the observed Fourier modes of the magnetic perturbations are summarized in table 2 in

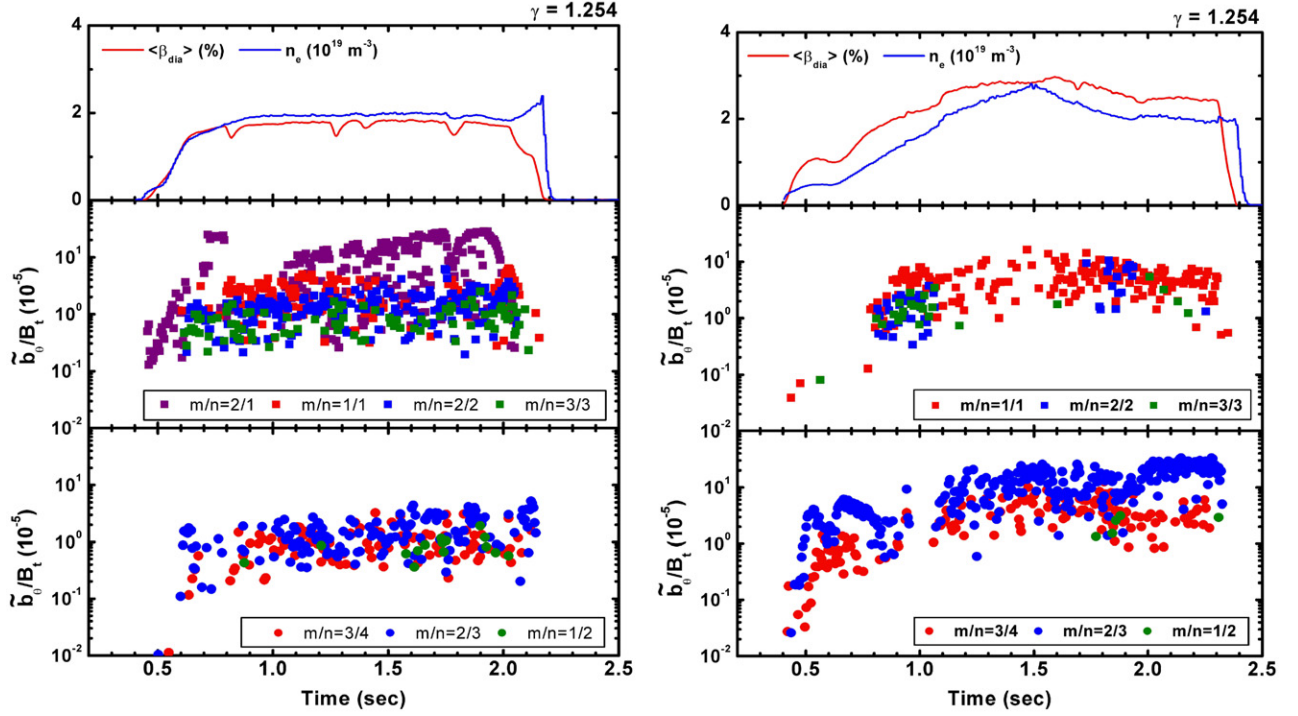


**Figure 1.** Time developments of the diamagnetic beta  $\langle \beta_{\text{dia}} \rangle$  (red line in the first row), line averaged electron density  $n_e$  (blue line in the first row) and Fourier decomposed perturbed poloidal field (root mean square in time interval of 10 ms) with  $n/m = 1/2, 1/1, 2/2, 3/3$  (the second row) and with  $n/m = 4/3, 3/2, 2/1$  (the third row) observed by the magnetic probes, for shot number 44238 (left column) and shot number 46465 (right column) in the inward-shifted LHD configuration with  $\gamma_c = 1.254$  [9].

**Table 1.**  $\langle \beta_{\text{dia}} \rangle$ -dependence of the experimentally observed Fourier modes of the perturbed magnetic field in the inward-shifted configuration with  $\gamma_c = 1.254$ . Note that  $n/m = 2/1$  modes sometimes observed are disregarded in this table [9–11].

Inward-shifted $\gamma_c = 1.254$		$(m, n)$			
$\langle \beta_{\text{dia}} \rangle \leq 1.0\%$	(2, 1)	(1, 1)(2, 2)(3, 3)	(3, 4)	(2, 3)	
$1.0\% \leq \langle \beta_{\text{dia}} \rangle \leq 2.0\%$	(2, 1)	(1, 1)(2, 2)(3, 3)	(3, 4)	(2, 3)	
$2.0\% \leq \langle \beta_{\text{dia}} \rangle \leq 2.5\%$		(1, 1)(2, 2)(3, 3)	(3, 4)	(2, 3)	
$2.5\% \leq \langle \beta_{\text{dia}} \rangle \leq 3.2\%$		(1, 1)(2, 2)(3, 3)	(3, 4)	(2, 3)	
$t = n/m$	0.5	1.0	1.3	1.5	

the inward-shifted configuration with  $\gamma_c = 1.220$  for such MHD equilibria that the currentless approximation is suitable ( $I_p/B_T \sim 10 \text{ kA T}^{-1}$ ). As well as the case for the configuration with  $\gamma_c = 1.254$ , note that all the Fourier modes indicated in table 2 are not necessarily observed in one shot. Which modes are observed depends on the experimental conditions as understood from figure 2.

It is understood from table 2 that (1) instabilities with  $n/m = 1/2$  excited in the plasma core region disappear as  $\beta$  increases as well as the configuration with  $\gamma_c = 1.254$ , (2) the higher harmonics are simultaneously excited at the plasma periphery with  $t = 1$  as well as the configuration with  $\gamma_c = 1.254$  and (3) instabilities resonating nearer the plasma edge ( $n/m = 2/1, 5/2$ ) are significantly excited together with the disappearance of instabilities resonating at  $t = 1$  as  $\langle \beta_{\text{dia}} \rangle$  increases, which is different from the configuration with  $\gamma_c = 1.254$ . Moreover, in the experimental results up to now, there is no indication that MHD activities by observed perturbations limit reachable  $\beta$  value for both inward-shifted configurations.

Properties of the observed MHD activities that (1) instabilities with  $n/m = 1/2$  in the core region disappear in high  $\beta$  plasmas, (2) instabilities near the plasma boundary are almost always excited independent of  $\beta$  values (instabilities resonating beyond the vacuum LCFS are excited as  $\beta$  increases for  $\gamma_c = 1.220$ ) and (3) there is no tendency of the  $\beta$  limit by MHD activities, must be closely related to the MHD equilibria. Since MHD equilibrium is determined by the three conditions, namely, the net toroidal current, the pressure profile and the boundary condition, such conditions must be considered from the experimental aspect as follows: MHD activities summarized in tables 1 and 2 are picked up from MHD equilibria with  $I_p/B_T \sim 10 \text{ kA T}^{-1}$ , so that the currentless condition becomes a good approximation [9]. There are experimentally standard observations that the stochastic magnetic region surrounding nested flux surfaces holds a temperature gradient, that is, the electron temperature gradient exists beyond the LCFS [7], and hollow electron density profiles are created especially in high- $\beta$  operations with a high NBI power and a low magnetic field, the hollowness of which is strengthened



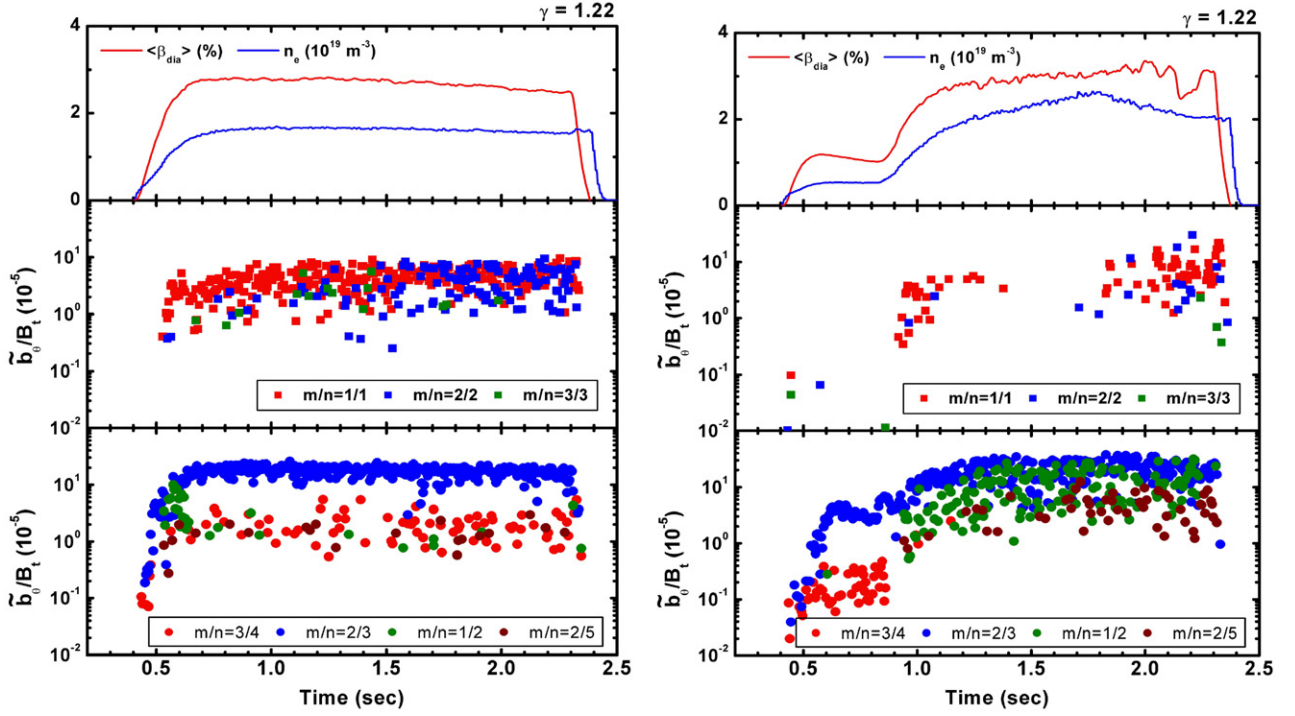


**Figure 2.** Time developments of the diamagnetic beta  $\langle \beta_{\text{dia}} \rangle$  (red line in the first row), line averaged electron density  $n_e$  (blue line in the first row) and the Fourier decomposed perturbed poloidal field (root mean square in time interval of 10 ms) with  $n/m = 1/1, 2/2, 3/3$  (the second row) and with  $n/m = 4/3, 3/2, 2/1, 5/2$  (the third row) observed by the magnetic probes, for shot number 46346 (left column) and shot number 46337 (right column) in the inward-shifted LHD configuration with  $\gamma_c = 1.220$  [9].

**Table 2.**  $\langle \beta_{\text{dia}} \rangle$ -dependence of the experimentally observed Fourier modes of the perturbed magnetic field in the inward-shifted configuration with  $\gamma_c = 1.220$  [9–11].

Inward-shifted $\gamma_c = 1.220$		$(m, n)$				
$\langle \beta_{\text{dia}} \rangle \leq 1.0\%$			(1, 1)(2, 2)(3, 3)	(2, 3)		
$1.0\% \leq \langle \beta_{\text{dia}} \rangle \leq 2.0\%$	(2, 1)		(1, 1)(2, 2)(3, 3)	(2, 3)		
$2.0\% \leq \langle \beta_{\text{dia}} \rangle \leq 2.5\%$	(2, 1)		(1, 1)(2, 2)(3, 3)	(2, 3)		
$2.5\% \leq \langle \beta_{\text{dia}} \rangle \leq 3.0\%$			(1, 1)(2, 2)(3, 3)	(2, 3)		
$3.0\% \leq \langle \beta_{\text{dia}} \rangle \leq 3.5\%$			(1, 1)(2, 2)(3, 3)	(2, 3)	(1, 2)	(2, 5)
$3.5\% \leq \langle \beta_{\text{dia}} \rangle \leq 4.3\%$				(2, 3)	(1, 2)	(2, 5)
$t = n/m$	0.5	1.0	1.5	2.0	2.5	

as the density increases [8]. In the high- $\beta$  operation in the inward-shifted LHD configuration, the low magnetic field with  $B \sim 0.5 \text{ T}$  is usually used and a high power NBI with beam energy 120–150 keV is introduced into a target plasma created by ECH. It might be expected that the orbit excursion of high energy ions is fairly large due to the high energy and the low magnetic field. The NBI does not act as beam fuelling. High- $\beta$  plasmas are achieved by introducing a gas puffing into NBI-heated plasmas from the first wall side. Introduction of cold neutral gas into a NBI-heated plasma leads to the formation of a hollow density profile through ionization and making the plasma near the stochastic field region cool down. Therefore, it is considered that the pressure profile is broad with a steep gradient near the plasma boundary and the plasma boundary is beyond the last close flux surface of the vacuum magnetic field. Comparing the equilibrium database with the pressure profile created by the measured hollow electron density profile  $n_e$ , the measured electron temperature  $T_e$  and the ion temperature assumed to be  $T_i \sim T_e$ , an essential factor of the pressure profile of high- $\beta$

plasmas in the inward-shifted LHD configuration is considered to be  $P(s) \sim P(0)(1 - s)$ , where  $s$  is the normalized toroidal flux and the plasma boundary ( $s = 1$ ) is considered to be beyond the vacuum LCFS.

Moreover, there are two gradient scales in the stochastic region, as is shown in figure 4 in [7] and the typical electron temperature in the region with a long gradient scale is around less than 50 eV. Introduction of cold neutral gas into a NBI-heated plasma makes the plasma near the stochastic field region cool down, leading to the two gradient scales of the electron temperature. As a result, low temperature and high density plasmas with a hollow density profile are created around or beyond the vacuum LCFS. For typical electron temperature (50 eV) and density ( $1 \times 10^{19} \text{ m}^{-3}$ ), the parallel mean free path  $\lambda_{\parallel}$  is around 3 m, which is smaller than the typical shortest vacuum connection length of 10 m in the stochastic region beyond the vacuum LCFS. Such a short connection length corresponds to the length of one poloidal turn of the magnetic field with  $t \sim 2$ . The pressure gradient beyond the vacuum LCFS is mainly determined by the parallel and perpendicular

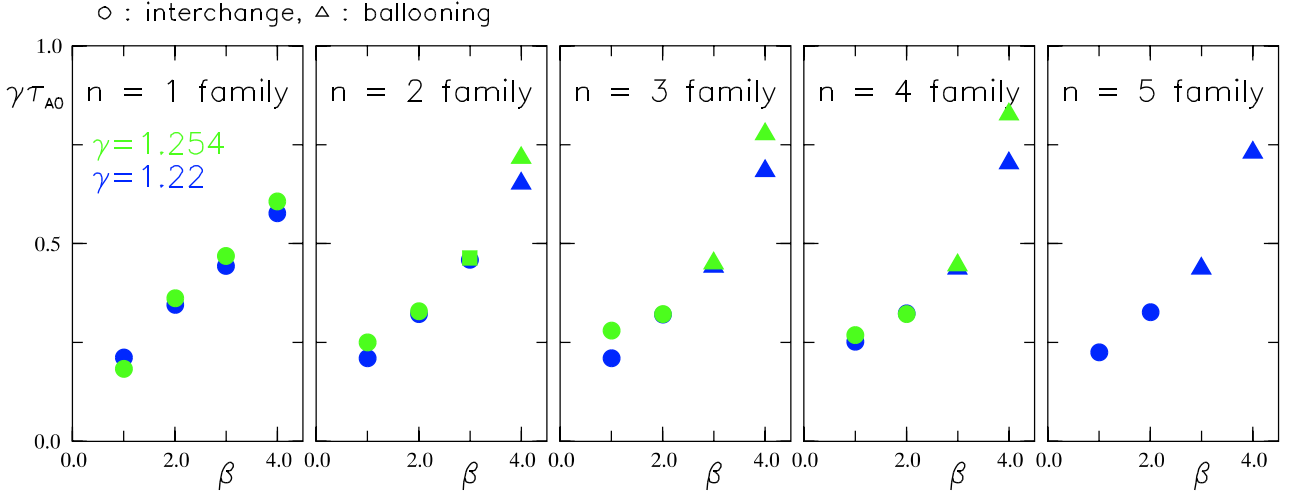


**Figure 3.** Normalized growth rate by the poloidal Alfvén transit time on the magnetic axis  $\gamma\tau_{A0}$  versus  $\beta$  for 5 mode families  $n_f = 1-5$ . Circles (triangles) indicate interchange (ballooning) modes. Green (blue) corresponds to  $\gamma_c = 1.254$  ( $\gamma_c = 1.220$ ). For  $\gamma = 1.254$ ,  $n_f = 5$  mode family is not calculated.

transport in such closed or open stochastic field lines. This situation determining the MHD equilibrium surrounded by the stochastic magnetic field lines is completely different from the determination of the tokamak MHD equilibrium with clear flux surfaces and separatrix.

Before starting LHD experiments, theoretical considerations on MHD stability are performed on the basis of the conjecture that the plasma does not expand beyond the clear vacuum LCFS, so that MHD equilibria are obtained under the fixed boundary condition determined from the clear vacuum LCFS [5], or free boundary MHD equilibria are obtained using an artificial material limiter determined from the clear vacuum LCFS at the outboard of the horizontally elongated poloidal cross section [6]. After LHD experiments, such conjecture on the plasma boundary has still been used, because to systematically determine the plasma boundary of high  $\beta$  plasma, reflecting the peripheral transport in the stochastic magnetic field region is very difficult from both the theoretical and the experimental points of view, except for some special cases (experimentally, reconstruction of the MHD equilibrium is possible in shot by shot). Only the experimental conditions related to the net toroidal current and the pressure profile are reflected to determine the MHD equilibria in the standard MHD stability analyses [3, 4]. Examples of such standard analyses based on the conjecture on the plasma boundary that the plasma does not expand beyond the clear vacuum LCFS are presented using fixed boundary currentless MHD equilibria with the pressure profile expressed as  $P(s) = P(0)(1-s)(1-s^\alpha)$ , where  $s$  is the normalized toroidal flux and  $\alpha$  is usually 4 or 9. The factor  $\alpha$  is introduced so as to eliminate the surface terms of the potential  $\delta W_s$  from the variational principle in the linearized ideal MHD stability analyses. One example of the standard linearized ideal MHD stability analyses with  $\alpha = 9$  is shown in figure 3, where the fixed boundary MHD equilibria are used in the inward-shifted LHD configurations with  $\gamma_c = 1.254$  and  $\gamma_c = 1.220$ . The rotational transforms at the plasma boundary are  $t_v = 1.48$  for  $\gamma_c = 1.254$  and  $t_v = 1.77$  for  $\gamma_c = 1.220$ . Both  $t_v$  are near the clear vacuum LCFS. Incompressible perturbations are assumed under the free boundary condition. The

**Table 3.**  $\beta$ -dependence of the most dominant Fourier modes in fixed boundary equilibria for vacuum boundary with  $t_v = 1.48$  for inward-shifted configuration with  $\gamma_c = 1.254$  (upper) and in fixed boundary equilibria for vacuum boundary with  $t_v = 1.77$  for inward-shifted configuration with  $\gamma_c = 1.220$  (lower).

$\gamma_c = 1.254$	Most dominant Fourier mode $(m, n)$ for each $n$				
$\beta = 1\%$	(2, 1)	(5, 2)	(8, 3)	(11, 4)	
$\beta = 2\%$	(2, 1)	(4, 2)	(6, 3)	(8, 4)	
$\beta = 3\%$	(2, 1)	(3, 2)	(5, 3)	(6, 4)	
$\beta = 4\%$	(2, 1)	(3, 2)	(4, 3)	(6, 4)	
$\gamma_c = 1.220$	Most dominant Fourier mode $(m, n)$ for each $n$				
$\beta = 1\%$	(2, 1)	(4, 2)	(6, 3)	(9, 4)	(11, 5)
$\beta = 2\%$	(2, 1)	(4, 2)	(6, 3)	(7, 4)	(9, 5)
$\beta = 3\%$	(2, 1)	(3, 2)	(5, 3)	(6, 4)	(8, 5)
$\beta = 4\%$	(2, 1)	(3, 2)	(4, 3)	(5, 4)	(6, 5)

growth rate  $\gamma$  is normalized by the poloidal Alfvén transit time defined as  $\tau_A \equiv \sqrt{\mu_0 \rho_m} / (2\pi t) dV/d\Phi_T$ , where  $\rho_m$ ,  $V$  and  $\Phi_T$  are the mass density, the plasma volume and the toroidal flux, respectively.

As  $\beta$  increases, the growth rates increase monotonically up to  $\gamma \sim 1/\tau_{A0}$  at  $\beta \sim 4\%$ . The corresponding most dominant Fourier modes for each toroidal mode number  $n$  are denoted in table 3 (see the section 5.2 for the classification by the toroidal mode number).

The discrepancy on MHD instabilities between experimental results and theoretical results is quite clear. In the case of used fixed boundary equilibria, the rational surface with  $t = 1/2$  does not disappear even if  $\beta$  increases, leading to the strong excitation of  $n/m = 1/2$  modes with the global radial structure. Moreover, monotonic increase of the growth rates up to  $\gamma \sim 1/\tau_{A0}$  with respect to  $\beta$  is unlikely to occur in the experiments; otherwise strong confinement degradation or  $\beta$  limit will be observed in high- $\beta$  experiments. Since the main difference of the MHD equilibria between theoretical analyses and experimental results is considered to be the treatment of the boundary condition between plasma and vacuum, properties of the peripheral magnetic field are investigated in the next section in order to relax the discrepancy on the MHD equilibria between experimental results and theoretical consideration.

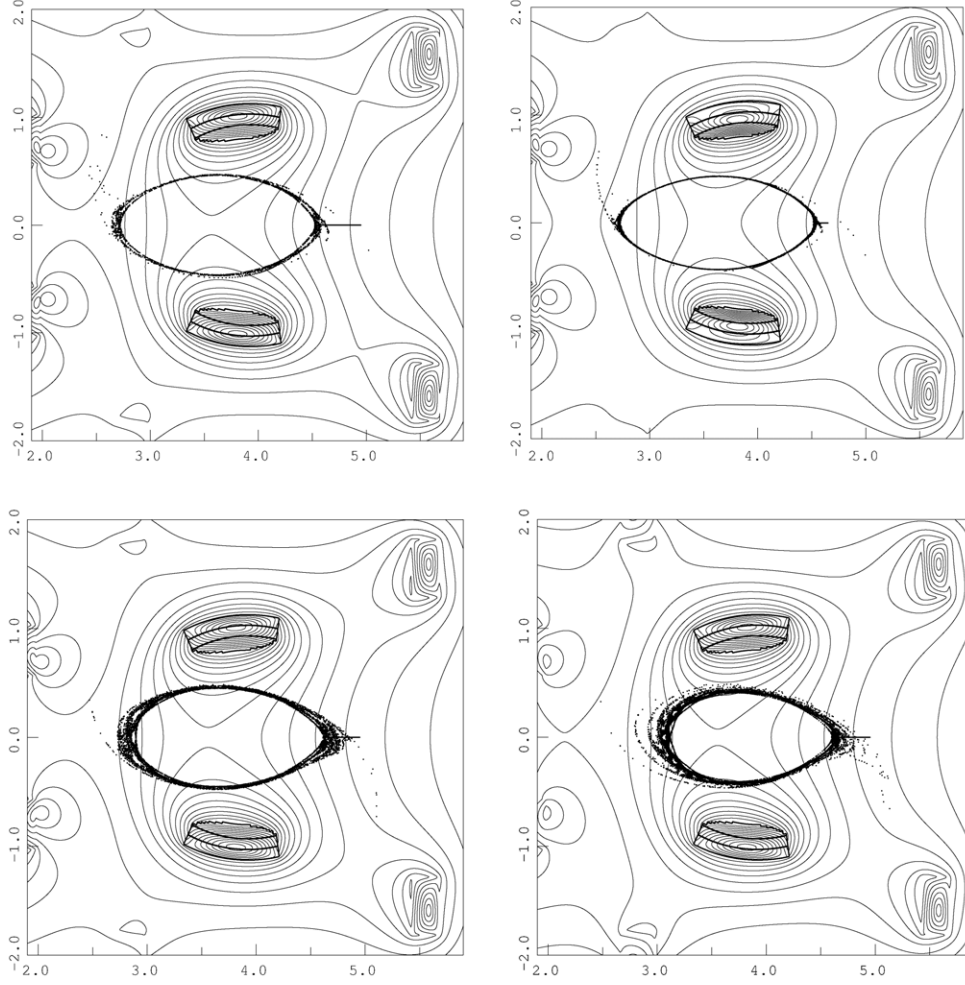


**Figure 4.** Poincaré plots of the peripheral vacuum magnetic field at the horizontally elongated LHD poloidal cross section for inward-shifted with  $\gamma_c = 1.254$  (upper left), inward-shifted with  $\gamma_c = 1.220$  (upper right), standard (lower left) and outward-shifted (lower right) configurations. In the Poincaré plots, the contours of the magnetic field strength and the shape of helical coils consisting of three layers are also shown by the thin and thick solid lines, respectively.

### 3. Consideration on MHD equilibria

#### 3.1. Properties of the peripheral magnetic field in vacuum

In order to consider more consistent MHD equilibria between experiments and theory, properties of the peripheral stochastic magnetic field in the inward-shifted LHD configuration are investigated, taking account of the experimental observation that the stochastic magnetic region surrounding nested flux surfaces holds confinement properties or temperature gradient [7]. In order to understand the properties of the peripheral stochastic magnetic field, the Poincaré plots of the peripheral vacuum magnetic field at the horizontally elongated LHD poloidal cross section are shown in figure 4, for inward-shifted with  $\gamma_c = 1.254$  (upper left), inward-shifted with  $\gamma_c = 1.220$  (upper right), standard (lower left) and outward-shifted (lower right) configurations. From these figures, it is understood that the width of the peripheral region with stochastic magnetic field lines changes from thick to thin according to the vacuum magnetic axis shift from outboard to inboard of the torus. The inward-shifted configuration is characterized as the configuration with the thinnest peripheral stochastic layer. Thus, it might be considered that the level of

the stochasticity or the degree of the perturbed magnetic field is smallest in the inward-shifted configuration compared with the standard and outward-shifted configurations.

Moreover, the width of the stochastic layer strongly depends on the coil inverse aspect ratio  $\gamma_c$ . The smaller coil inverse aspect ratio makes a thinner stochastic layer. The helical coils of LHD are wound with such a pitch modulation as to make the plasma volume large, as is understood from the relative position of the helical coils in the poloidal cross section. Thus, inward-shift of the vacuum magnetic axis means the recovery of the helical symmetry under the pitch modulation of helical coils to some extent. This recovery of the helical symmetry is strengthened by the smaller coil inverse aspect ratio. The corresponding connection length (toroidal turn)  $L_c$  and vacuum rotational transform  $t_v$  are shown in figure 5 for the inward-shifted LHD configuration with  $\gamma_c = 1.254$  (left) and  $\gamma_c = 1.220$  (right).

The lower rows of figure 5 indicate that the connection length (toroidal turn) of the magnetic field lines started from the equatorial plane ( $z = 0$ ) as a function of the major radius  $R$ . The corresponding vacuum rotational transform  $t_v$  is denoted in the upper rows of figure 5, where  $t_v$  is set 0 when the

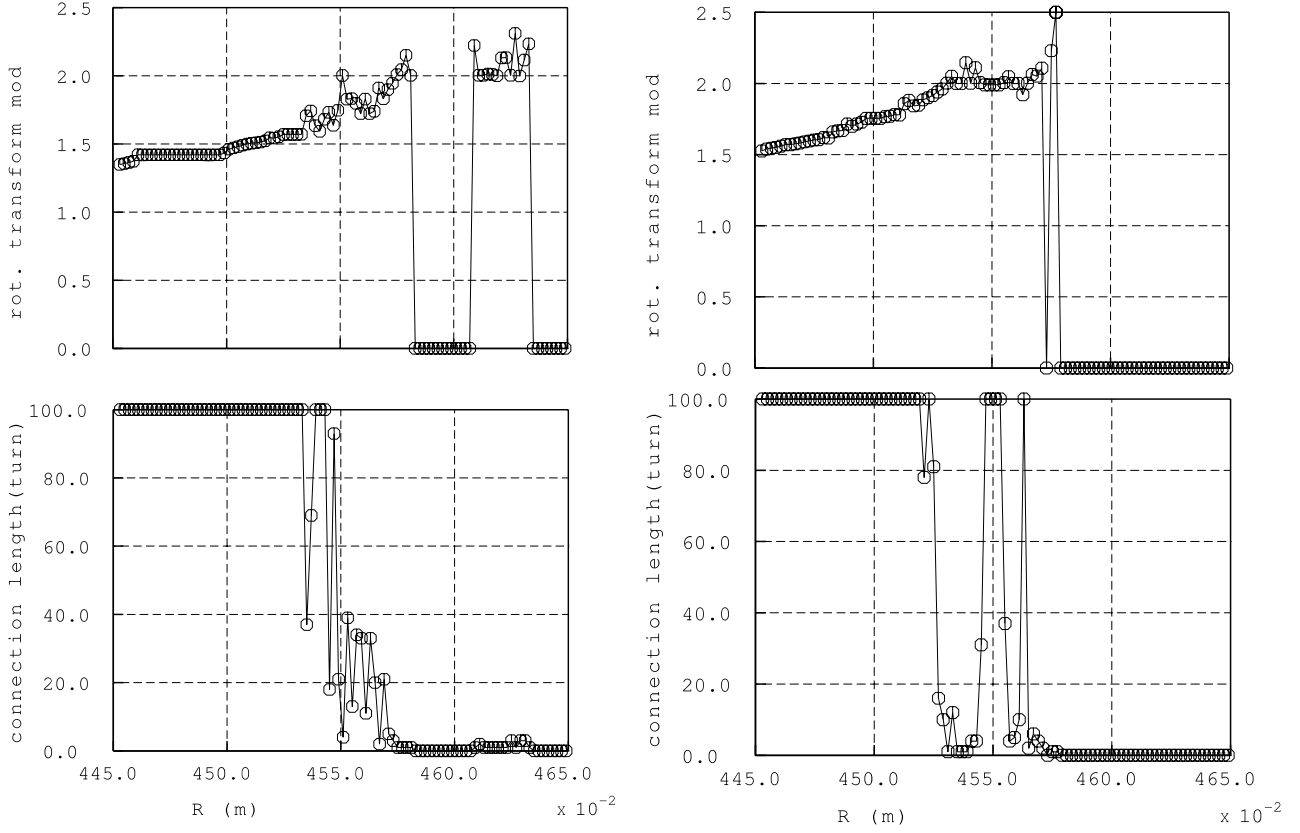


**Figure 5.** The vacuum rotational transform  $t_v$  (upper rows) and the connection length (toroidal turn)  $L_c$  (lower rows) as a function of the major radius  $R$  for inward-shifted LHD configuration with  $\gamma_c = 1.254$  (left columns) and with  $\gamma_c = 1.220$  (right columns) corresponding to figure 4.

**Table 4.** Characteristics of the peripheral magnetic field of the inward-shifted LHD configuration corresponding to figures 4 and 5 for  $\gamma_c = 1.254$  and  $\gamma_c = 1.220$ , where  $t_v$  and  $L_c$  are the vacuum rotational transform and the connection length of the magnetic field lines.

$\gamma_c = 1.254$		$\gamma_c = 1.220$	
Range of $t_v$	Character of $L_c$	Range of $t_v$	Character of $L_c$
$t_v \lesssim 1.48$	Clear flux surfaces	$t_v \lesssim 1.78$	Clear flux surfaces
$1.48 < t_v \lesssim 1.58$	Long $L_c$	$1.78 \lesssim t_v \lesssim 1.85$	Long $L_c$
$1.58 < t_v \lesssim 2.00$	Short $L_c$	$1.85 \lesssim t_v \lesssim 2.00$	Short $L_c$
$2.00 < t_v$	Very short $L_c$	$t_v = 2.00$	Clear islands
		$2.00 \lesssim t_v \lesssim 2.50$	Short $L_c$
		$2.50 \lesssim t_v$	Very short $L_c$

connection length is shorter than one toroidal turn. From these two types of figures, it is understood that the region with a fairly long connection length (more than 100 toroidal turns  $\sim 2.2$  km) is limited by magnetic islands with  $t_v = 30/19 \sim 1.58$ , and a clear LCFS might be chosen around  $t_v = 1.48$  near the magnetic island with  $t_v = 30/20$  in the inward-shifted configuration with  $\gamma_c = 1.254$ . This tendency does not change even if magnetic field lines are followed more, for example, 1000 toroidal turns  $\sim 22$  km. The properties of the peripheral magnetic field are summarized in table 4. In the case of the configuration with  $\gamma_c = 1.220$ , clear magnetic islands with  $t = 2.0$  exist. The rotational transform of the separatrix of the straight helical with  $M = 10$  and  $L = 2$  is  $5 = M/L$ . Recovery of the helical symmetry in the configuration with  $\gamma_c = 1.220$  leads to the existence of the stiff magnetic islands. This stiffness of the peripheral magnetic field might be related

to exciting the perturbation with Fourier modes resonating at high rotational transforms beyond LCFS, namely  $t = 2, 2.5$ , in table 2.

### 3.2. Properties of the peripheral magnetic field in finite $\beta$ equilibria

Even if there is no net toroidal current, there is a case while the Pfirsch–Schlüter current changes the magnetic field structure significantly. In the case of planar axis heliotron configuration like LHD, the Pfirsch–Schlüter current has fairly large axisymmetric components and small non-axisymmetric components. The former makes a large Shafranov shift in the major radius direction, and the latter leads to a formation of magnetic islands and stochastic regions or healing of magnetic islands [15]. Properties of the peripheral magnetic field of finite- $\beta$  MHD equilibria are investigated using HINT2 code



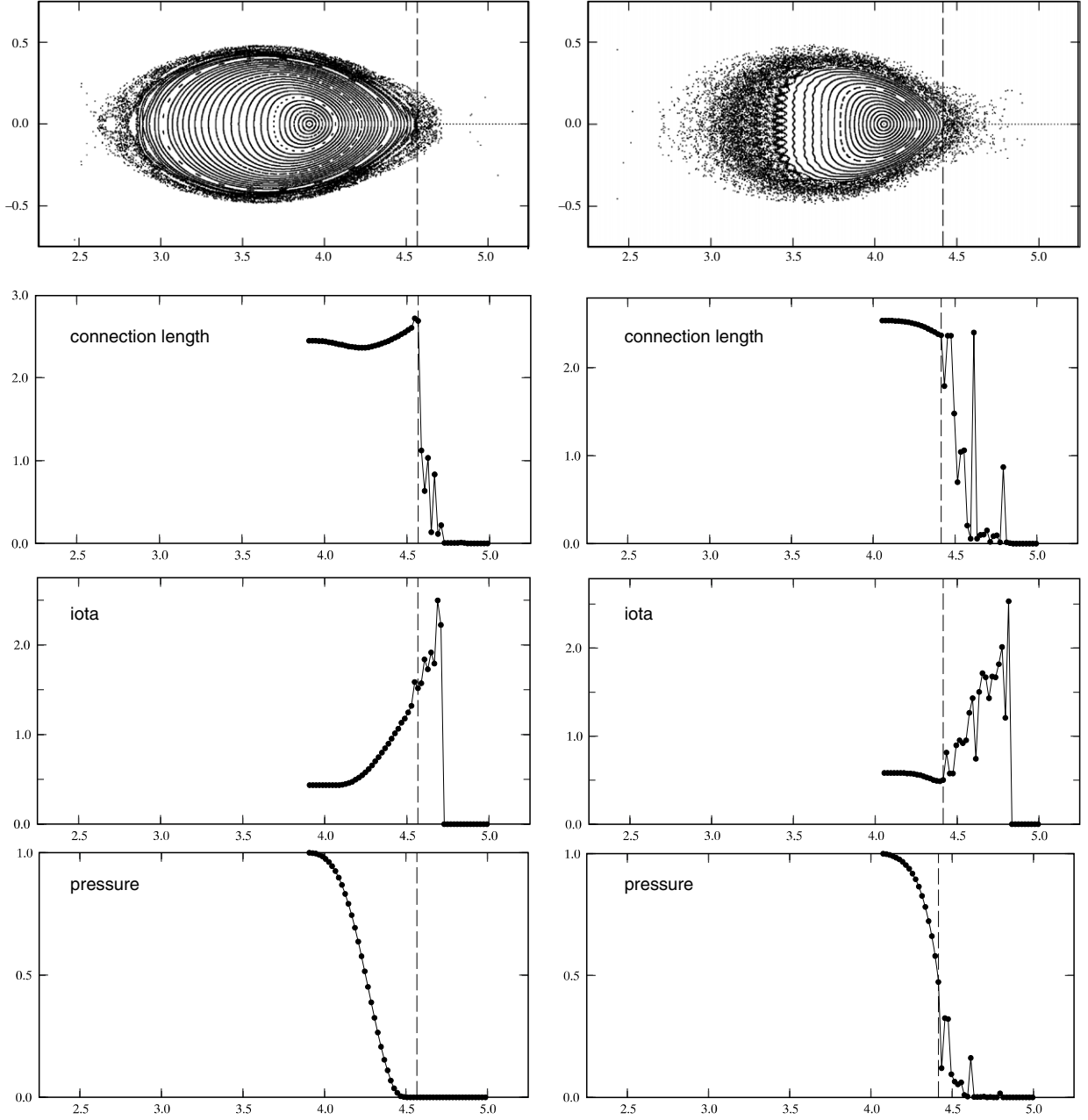


**Figure 6.** Poincaré plots of the magnetic field lines in the horizontally elongated LHD poloidal cross section (the first rows), and the corresponding connection length  $L_c/10^3$  m (the second rows), rotational transform  $\iota$  (the third rows) and pressure  $P$  for  $\beta = 1.8\%$  (the first columns) and  $\beta = 3.6\%$  (the second columns) versus the major radius  $R$  in the inward-shifted LHD configuration with  $\gamma_c = 1.254$ . The vertical dotted line indicates the position near the last close flux surface.

(a new version of the original HINT code [16]). Although the boundary of the calculation box of HINT or HINT2 is assumed to be a perfect conductor, the obtained MHD equilibrium is a free boundary equilibrium because no fixed boundary condition is introduced between the plasma region and the vacuum region. Figure 6 shows the Poincaré plots of the magnetic field lines (the first rows), the connection length  $L_c/10^3$  m (the second rows), the rotational transform  $\iota$  (the third rows) and the pressure profile  $P$  as a function of the major radius  $R$  for  $\beta = 1.8\%$  (the first columns) and  $\beta = 3.6\%$  (the second columns) in the inward-shifted configuration with  $\gamma_c = 1.254$ , where the initial pressure

profile for HINT2 is chosen as  $P(s) = P_0(1 - s)(1 - s^4)$ . The final pressure profile is similar to the initial profile but not the same.

As  $\beta$  increases, the width of the peripheral magnetic islands becomes wide, and a stochastic magnetic field is created near the plasma periphery through island-overlapping. Such a stochastic region penetrates from the plasma peripheral region to the core region, as  $\beta$  increases. The same figures are shown in figure 7 for the inward-shifted configuration with  $\gamma_c = 1.220$ . Comparing figures 6 and 7, it is understood that the Shafranov shift is fairly large even in low- $\beta$  and that the Shafranov shift in the configuration with

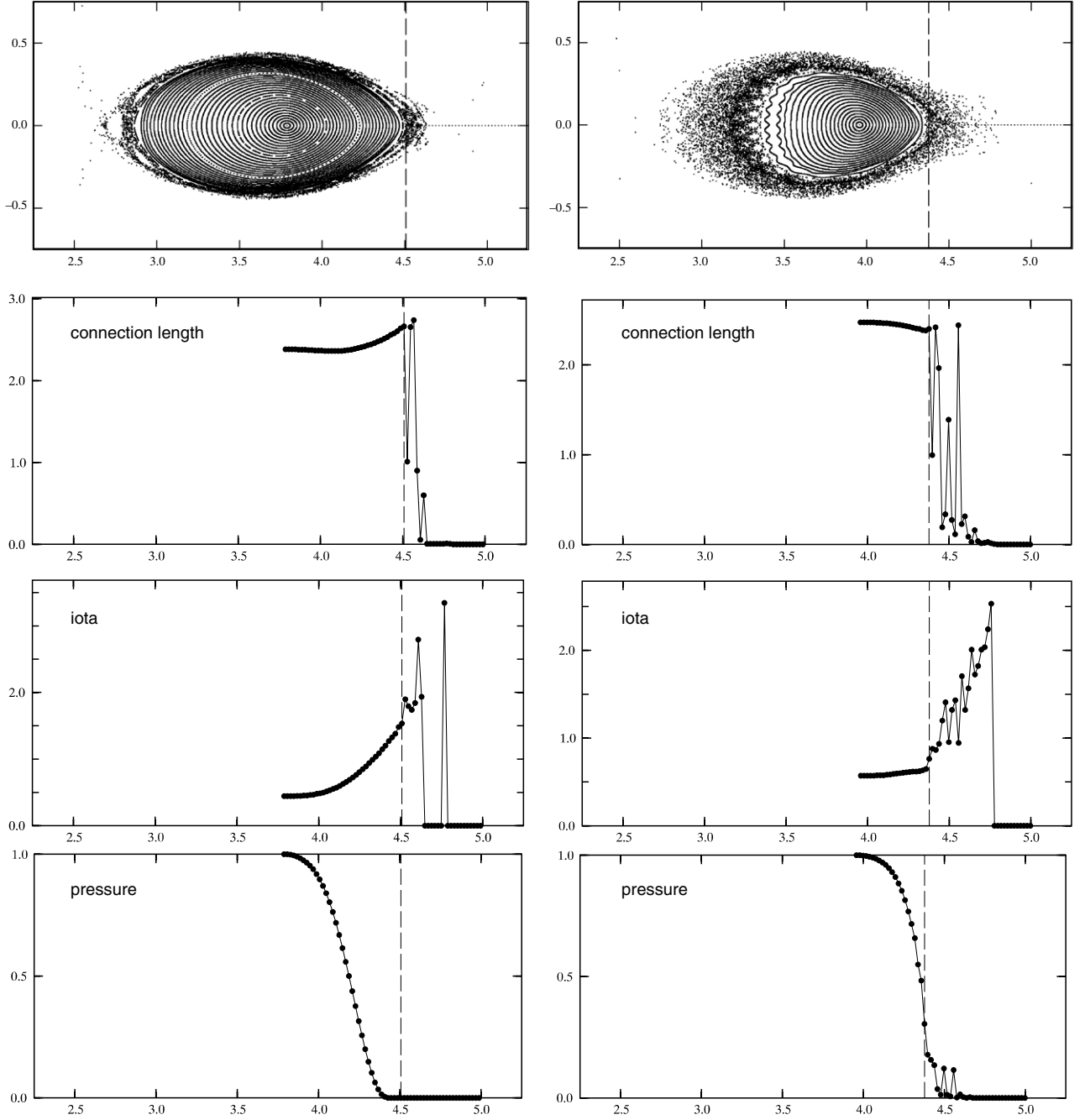


**Figure 7.** Poincaré plots of the magnetic field lines in the horizontally elongated LHD poloidal cross section (the first rows), and the corresponding connection length  $L_c$  (the second rows), rotational transform  $t$  (the third rows) and pressure  $P$  for  $\beta = 1.8\%$  (the first columns) and  $\beta = 3.5\%$  (the second columns) versus the major radius  $R$  in the inward-shifted LHD configuration with  $\gamma = 1.220$ . The vertical dotted line indicates the position near the last close flux surface.

$\gamma_c = 1.220$  is smaller than that in the configuration with  $\gamma_c = 1.254$ .

In both configurations, the pressure almost vanishes and the rotational transform  $t$  has a value similar to that in the vacuum at the LCFS when  $\beta$  is relatively low. As  $\beta$  increases, although the pressure and pressure gradient still remain in the stochastic region with a fairly long connection length, LCFS shrinks (the position of  $R$  of the LCFS outside the torus denoted by the dotted line moves inwardly, as is shown in figures 6 and 7) and the rotational transform  $t$  at the LCFS becomes quite

low, as is understood from the comparison between low- $\beta$  and high- $\beta$  equilibria in figures 6 and 7.

These properties are closely related to the HINT or HINT2 algorithm. In the HINT2, as well as the HINT code, a relaxation method is used in order to obtain the MHD equilibrium without the assumption of the nested flux surfaces. The relaxation method is an iterative method consisting of (1) parallel relaxation of the pressure along fixed magnetic field lines and (2) perpendicular relaxation of the magnetic field for the fixed pressure profile. In the parallel relaxation process of

the pressure, the values of the pressure  $P$  on all the Eulerian grid points ( $u^1, u^2, u^3$ ) are replaced by the averaged values using field line tracing. Moreover, when the turn number of the magnetic field line in the toroidal direction is typically smaller than one, the pressure at the starting grid is replaced by 0. Thus, when the level of stochasticity becomes higher according to  $\beta$ , the number of toroidal turns becomes less than one at many grid points, leading to a strong reduction of the pressure in the stochastic region. Corresponding to the pressure deformation, the rotational transform  $\iota$  at the LCFS is significantly reduced as  $\beta$  increases.

In the HINT code, physical transport processes are not included, but non-physical transport process is included in such a way that the value of pressure on the grid points is replaced by 0 when the field line on the grid reaches the calculation box in less than one toroidal turn. This process is interpreted as a very fast parallel thermal transport process that the pressure will be lost very quickly, namely  $\chi_{\parallel} \rightarrow \infty$ , when the magnetic field lines reach the wall in less than one toroidal turn. Thus, the present algorithm of HINT or HINT2 is not applicable to inward-shifted LHD experiments with the experimental observation that the pressure gradient still survives in the stochastic magnetic field beyond the vacuum LCFS. Moreover, even in the algorithm used in [17, 18], the similar shrink of the LCFS might be expected in the case of LHD, because the transport process in the stochastic magnetic region is not included. Improvement of the HINT algorithm so as to include the peripheral transport process is now underway. The function in the parallel relaxation of the pressure for fixed magnetic field in the present HINT or HINT2 is expressed as

$$P_{\text{new}}(\vec{x}) = \frac{\int_{\vec{x}}^{\vec{x}_{\text{end}}} \mathcal{F} P_{\text{old}}(dl/B)}{\int_{\vec{x}}^{\vec{x}_{\text{end}}} (dl/B)}, \quad (1)$$

where  $dl$  is the line element along the magnetic field line starting from  $\vec{x}$  and  $\mathcal{F}$  is a weight function:

$$\mathcal{F} = \begin{cases} 1 & \text{for } |u_{\text{end}}^3 - u^3| \geq 2\pi, \\ 0 & \text{for } |u_{\text{end}}^3 - u^3| < 2\pi, \end{cases} \quad (2)$$

where  $u^3$  and  $u_{\text{end}}^3$  are the toroidal angles at the starting point  $\vec{x}$  and ending point  $\vec{x}_{\text{end}}$ , respectively. Thus, by changing the weight function  $\mathcal{F}$  as a function of the connection length or the number of toroidal turns, taking account of the transport in the stochastic region, we might introduce the transport in the stochastic magnetic field region into the MHD equilibrium. As a more complicated way, introducing an anisotropic pressure is also considered. These results will be presented elsewhere.

### 3.3. Determination of MHD equilibria

Even if the facts that a small change of the pressure profile keeping the key factor  $(1 - s)$  alters the stability properties and that the range of the observed Fourier modes is limited are taken into account, the discrepancy on MHD stability between experimental results and standard ideal MHD analyses based on the fixed boundary MHD equilibria cannot be removed. Especially, a significant monotonic increase in the linear growth rate with  $\beta$  and disappearance of  $n/m = 1/2$  modes in high  $\beta$  plasma cannot be explained in the framework of the

standard stability analyses based on the fixed boundary MHD equilibria. In order to remove the discrepancy, more correct treatment of the plasma boundary should be considered. On the other hand, the plasma boundary surrounded by the stochastic magnetic field is considered to be essentially determined by the transport in the stochastic region including open magnetic field lines. In the three-dimensional configuration without toroidal symmetry, the determination of the plasma boundary by the transport is very complicated compared with tokamaks with clear flux surfaces and separatrix. Since, at present, the clear systematic way of how to experimentally or theoretically determine the plasma–vacuum boundary is not established (indeed, the trail to introduce the transport process into equilibrium code HINT2 has just started), the concept of averaged flux surfaces is introduced. The averaged flux surfaces are defined in the stochastic magnetic field region as surfaces with a long connection length compared with the parallel mean free path, a definite rotational transform and a small electron thermal conductivity. The averaged flux surfaces are assumed to exist in the region with the stochastic magnetic field in order to take into account the experimental fact that the pressure gradient exists beyond the vacuum LCFS [7, 8]. Such averaged flux surfaces are considered to be created by the synergetic effects between the change of the magnetic field in the stochastic region by the plasma Pfirsch–Schlüter current and transport process in the stochastic region. Once such averaged flux surfaces are assumed to exist, then plasma could move into such averaged flux surfaces in order to take the MHD force balance, which allows the boundary modulation, namely change of the boundary shape and shift of the boundary. As is understood from the optimization of the three-dimensional system, the boundary modulation will bring significant effects to MHD stability.

Plasma motion based on the averaged flux surfaces will be realized by the free boundary MHD equilibrium calculation assuming the nested flux surfaces. Since there is no clear information on the total toroidal flux inside the plasma, several vacuum boundaries are chosen under the assumption that the total toroidal flux is conserved, taking account of the information of the vacuum peripheral magnetic field and the experimental fact that pressure gradient exists beyond the vacuum LCFS [7, 8]. For the inward-shifted LHD configuration with  $\gamma_c = 1.254$ , three different plasma boundaries are chosen from a clear vacuum flux surface with  $t_v = 1.48$ , near the vacuum LCFS with  $t_v = 1.58$  and outside the vacuum LCFS with  $t_v = 1.72$ , and for the inward-shifted configuration with  $\gamma_c = 1.220$ , three different plasma boundaries are chosen from a clear vacuum flux surface with  $t_v = 1.77$ , near the vacuum LCFS with  $t_v = 1.83$  and outside the vacuum LCFS with  $t_v = 2.19$ . The corresponding minimum and maximum positions in the major radius direction,  $R_{\min}$  and  $R_{\max}$ , at the horizontally elongated poloidal cross section are  $R_{\min} = 2.75$  (m) and  $R_{\max} = 4.50$  (m) for  $t_v = 1.48$ ,  $R_{\min} = 2.72$  (m) and  $R_{\max} = 4.52$  (m) for  $t_v = 1.58$  and  $R_{\min} = 2.68$  (m) and  $R_{\max} = 4.56$  (m) for  $t_v = 1.72$ , respectively, for the inward-shifted configuration with  $\gamma_c = 1.254$ . For the inward-shifted configuration with  $\gamma_c = 1.220$ ,  $R_{\min} = 2.74$  (m) and  $R_{\max} = 4.51$  (m) for  $t_v = 1.77$ ,  $R_{\min} = 2.73$  (m) and  $R_{\max} = 4.52$  (m) for  $t_v = 1.83$

and  $R_{\min} = 2.65$  (m) and  $R_{\max} = 4.58$  (m) for  $t_v = 2.19$ , respectively. Hereafter, MHD equilibria are distinguished by the vacuum rotational transform at the plasma–vacuum boundary  $t_v$  and the inverse coil aspect ratio  $\gamma_c$ .

According to the experimental observation discussed in the previous section, the currentless condition and the pressure profile  $P(s) = P_0(1-s)(1-s^\alpha)$  with  $\alpha = 9$  are used, where  $s$  is the normalized toroidal flux, which is related to the normalized minor radius  $\rho$  as  $s = \rho^2$ . The coefficient  $P_0$  is controlled in the changing  $\beta$  value. As discussed in the previous section, the essential form of the experimentally obtained pressure profile is  $P(s) \sim P(0)(1-s)$ . The factor  $(1-s)$  in the expression of  $(1-s^\alpha)$  is introduced in order to remove the surface potential term of  $\delta W_s$  in the variational principle, because  $\delta W_s$  is not included in cas3d3 [14]. The power of  $\alpha = 9$  in the expression of  $(1-s^\alpha)$  is chosen in order to keep the fairly steep pressure gradient near the plasma boundary. When  $\alpha$  is decreased, say  $\alpha = 4$ , the pressure gradient near the plasma boundary decreases, which will increase the discrepancy between experimental observations and theoretical consideration. In the case of  $\alpha = 4$ , however, the qualitative properties do not change from the case with  $\alpha = 9$ .

The free boundary MHD equilibria are calculated using vmec code [13]. The resultant free boundary MHD equilibria have the extended minimum and maximum positions in the major radius direction at the horizontally elongated poloidal cross section. For  $\beta = 4\%$  in the inward-shifted configuration with  $\gamma_c = 1.254$ ,  $R_{\min} = 2.90$  (m) and  $R_{\max} = 4.77$  (m) for  $t_v = 1.48$ ,  $R_{\min} = 2.87$  (m) and  $R_{\max} = 4.79$  (m) for  $t_v = 1.58$  and  $R_{\min} = 2.82$  (m) and  $R_{\max} = 4.83$  (m) for  $t_v = 1.72$ , respectively. For  $\beta = 4\%$  in the inward-shifted configuration with  $\gamma_c = 1.220$ ,  $R_{\min} = 2.86$  (m) and  $R_{\max} = 4.74$  (m) for  $t_v = 1.77$ ,  $R_{\min} = 2.84$  (m) and  $R_{\max} = 4.75$  (m) for  $t_v = 1.83$  and  $R_{\min} = 2.78$  (m) and  $R_{\max} = 4.80$  (m) for  $t_v = 2.19$ , respectively. Comparing  $R_{\min}$  and  $R_{\max}$  between the vacuum and the finite- $\beta$  equilibria with  $\beta = 4\%$ , it is understood that the whole plasma including the boundary moves outwardly. These maximum positions  $R_{\max}$  are fairly outside the LCFS determined from the vacuum magnetic field in figure 5, however, they are still included in the experimentally obtained plasma region [7].

The obtained MHD equilibria might be valid for the stability analyses for low- $n$  modes with  $n < M$ , because the minimum toroidal mode number of the rational surfaces with magnetic islands is the same as the toroidal field period  $M (= 10)$  of the LHD. High-mode-number modes with  $n \gg M$  will be affected by the fine structure of the magnetic islands. In order to distinguish effects of the boundary modulation of the free boundary MHD equilibrium on MHD stability from stability properties in the fixed boundary MHD equilibria without the boundary modulation, MHD equilibria under the fixed boundary condition are created, where the plasma–vacuum boundary in the stochastic magnetic field region is determined from the boundary of the free boundary MHD equilibrium with quite a low plasma pressure. Note that for sufficiently small pressure, the whole plasma hardly moves even for free boundary condition.

#### 4. Properties of boundary spectra

MHD equilibria assuming the nested flux surfaces are described by the magnetic coordinates  $(s, \theta, \zeta)$ , where  $\theta$  and  $\zeta$  are poloidal and toroidal angles, respectively. Using the double periodicity in both poloidal and toroidal directions, the plasma boundary is Fourier decomposed as

$$\begin{aligned} R(\theta, \zeta) &= R_{mn} \cos(m\theta + n\zeta), \\ Z(\theta, \zeta) &= Z_{mn} \sin(m\theta + n\zeta), \end{aligned} \quad (3)$$

where  $m$  and  $n = Mi$  are poloidal and toroidal mode numbers, respectively, and  $M (= 10)$  for LHD is the toroidal field period and  $i$  is an integer. In the case of vmec code,  $\zeta$  is the geometrical angle of the cylindrical coordinates  $(R, \varphi, Z)$ , namely,  $\zeta = \varphi$ . Since the Fourier spectrum of the boundary does not change for the fixed boundary MHD equilibria as  $\beta$  increases, the change of the Fourier spectrum of the boundary in the free boundary MHD equilibrium clearly reflects the change in the properties of the whole Fourier spectrum by the free boundary motion of the equilibrium plasma. Figure 8 shows how the dominant Fourier components, except for  $(m, n) = (0, 0)$  and  $(m, n) = (1, 0)$  modes, change according to the  $\beta$  value in three MHD equilibria with different plasma–vacuum boundaries denoted by  $t_v$  for the inward-shifted configuration with  $\gamma_c = 1.254$ . Independent of the choice of the vacuum boundary, Fourier spectra of the plasma boundary show similar changes, which are brought about by a Shafranov shift of a whole plasma. The most significant changes appear in poloidally symmetric components denoted by blue symbols in figure 8.

To clarify the cause of the change in the poloidally symmetric components shown in figure 8, dominant boundary spectra of vacuum configurations with different vacuum magnetic axes  $R_{va}$  are drawn in figure 9. Changes of the boundary spectrum by vacuum magnetic axis shift mainly appear in poloidally symmetric components with  $(m, n) = (0, \neq 0)$ , as well as those by a large Shafranov shift in the inward-shifted configuration shown in figure 8. It is understood from the comparison between figures 8 and 9 that, in the inward-shifted LHD configurations, the vacuum flux surfaces are so compressed into the helical coils at the inner side of torus by the external coil current that the poloidally symmetric deformation of the plasma boundary is strongly enhanced. As  $\beta$  increases, the whole plasma moves from the inner side of the torus to the outer side. Through this Shafranov shift, the enforced boundary shaping by the external coil current will be so reduced that the poloidally symmetric deformation of the plasma boundary will diminish. In other words, a large internal plasma current (Pfirsch–Schlüter current) makes the opposite deformation of the boundary to that by the external coil current. These properties in the inward-shifted configuration with  $\gamma_c = 1.254$  hold in the inward-shifted configuration with  $\gamma_c = 1.220$ .

#### 5. Properties of the ideal MHD stability in the inward-shift LHD configurations

In the previous section, it is shown that free boundary motion of the equilibrium plasma significantly changes the



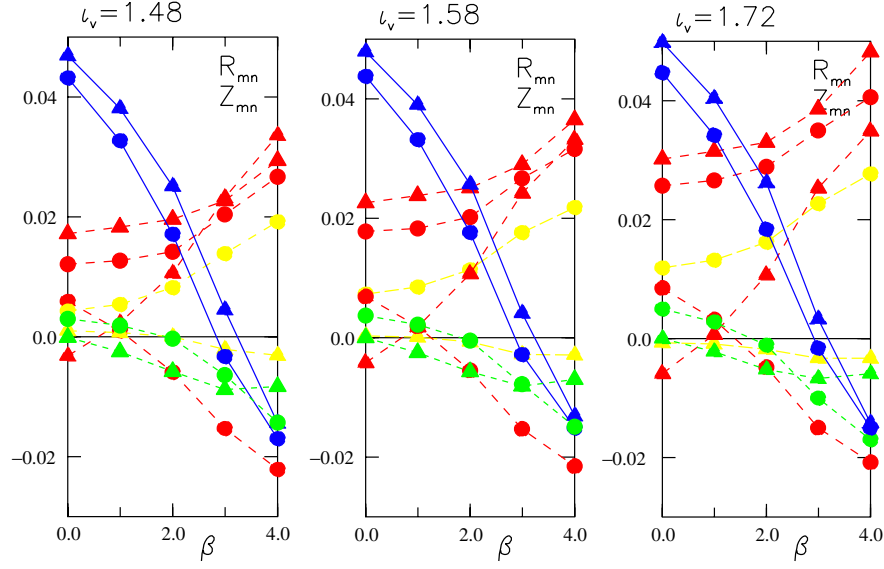


**Figure 8.**  $\beta$ -dependence of dominant boundary spectra, except for  $(m, n) = (0, 0)$  and  $(m, n) = (1, 0)$ , for three MHD equilibria with different vacuum boundaries, namely,  $t_v = 1.48$  (the first column),  $t_v = 1.58$  (the second column) and  $t_v = 1.72$  (the third column) in the inward-shifted configuration with  $\gamma_c = 1.254$ . Triangles and circles indicate  $Z_{mn}$  and  $R_{mn}$  components in equation (3). Blue, red, green and yellow symbols denote poloidally symmetric components with  $(m, n) = (0, \neq 0)$ , components with  $(m, n) = (\neq 0, 10)$ , axisymmetric components with  $(m, n) = (\neq 0, 0)$  and components with  $(m, n) = (\neq 0, 20)$ , respectively. Note that in MHD equilibria with the fixed boundary, the boundary spectra do not change with  $\beta$ , and the boundary spectra correspond to the case of  $\beta = 0$  in these graphs.

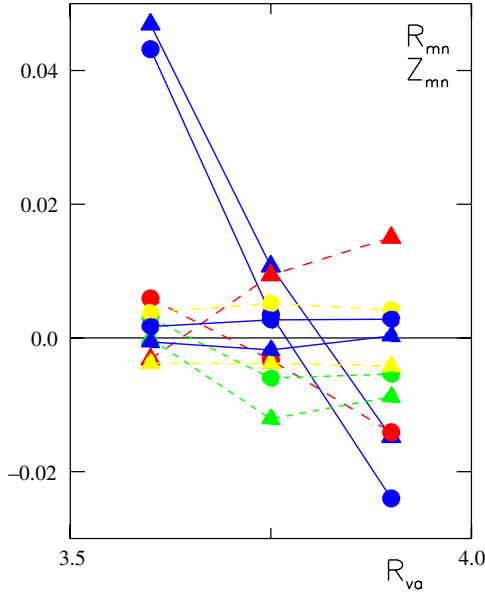


**Figure 9.** Vacuum magnetic axis  $R_{va}$  dependence of dominant boundary Fourier spectra except for  $(m, n) = (0, 0)$  and  $(m, n) = (1, 0)$ . Three vacuum configurations, namely, inward-shifted with  $R_{va} = 3.6$  m with  $\gamma_c = 1.254$ , standard with  $R_{va} = 3.75$  m, outward-shifted with  $R_{va} = 3.9$  m configurations are used. Triangles and circles indicate  $Z_{mn}$  and  $R_{mn}$  components in equation (3). Blue, red, green and yellow symbols denote poloidally symmetric components with  $(m, n) = (0, \neq 0)$ , components with  $(m, n) = (\neq 0, 10)$ , axisymmetric components with  $(m, n) = (\neq 0, 0)$  and components with  $(m, n) = (\neq 0, 20)$ , respectively.

boundary spectrum or makes the boundary modulation, which means that the geometrical influences on MHD stability might change significantly. Indeed, the optimization of the three-dimensional magnetic configuration has been done by

controlling the boundary shape [12]. In the case of the planar axis Heliotron configurations with a large Shafranov shift or a large internal current (Pfisch–Schlüter current), not only the external coil current but also internal plasma current changes the boundary shift and the boundary shape so much that the resultant MHD stability significantly depends on the boundary modulation. To see how much the boundary modulation of MHD equilibrium influences the MHD stability, linearized ideal MHD stability analyses are performed.

### 5.1. Effects of boundary modulation on equilibrium quantities

The influences of the boundary modulations of MHD equilibria on equilibrium quantities are examined. Figure 10 shows the  $\beta$ -dependences of the rotational transform  $t$  (the first columns), the magnetic well  $V'(\rho)/V'(0) - 1$  (the second columns) and the Mercier criterion  $D_I$  (the third columns) for fixed (the first rows) and free (the second rows) boundary MHD equilibrium with vacuum rotational transform at the boundary being  $t_v = 1.48$  in the inward-shifted configuration with  $\gamma_c = 1.254$  and for free boundary MHD equilibrium with  $t_v = 1.83$  in the inward-shifted configuration with  $\gamma_c = 1.220$  (the third rows), where  $V$  is the plasma volume and  $V' \equiv dV/ds$ . In other equilibria with different  $t_v$  in two inward-shifted configurations, the properties shown in figure 10 do not change qualitatively. There are two main crucial differences between MHD equilibria with the fixed boundary and those with free boundary, from the aspect of MHD stability. One is the  $\beta$ -dependence of  $t$ , and the other is  $\beta$ -dependence of  $D_I$ . The rotational transform  $t$  does not change so much in the fixed boundary MHD equilibria. In contrast, in the free boundary equilibria,  $t$  changes so significantly due to the whole plasma motion that the dangerous low rational surface with  $t = 1/2$  disappears, as  $\beta$  increases, which is consistent with the experimental observation given in tables 1 and 2.

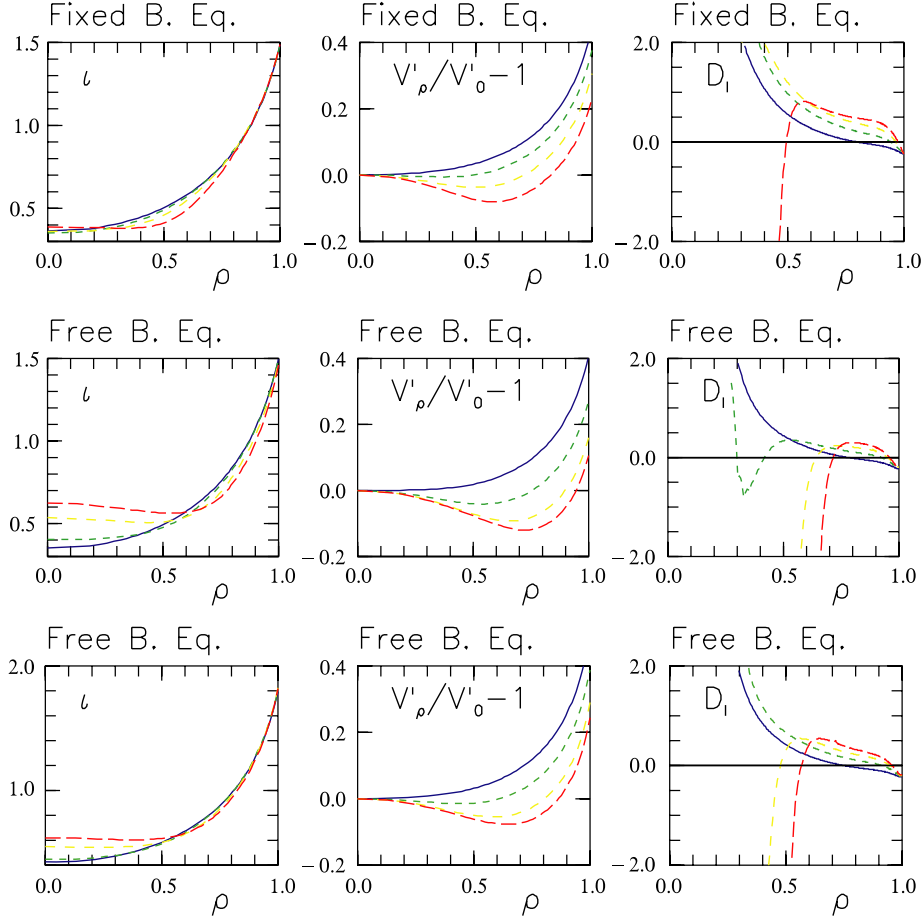


**Figure 10.**  $\beta$ -dependences of the rotational transform  $\iota$  (the first columns), the magnetic well  $V'(\rho)/V'(0) - 1$  (the second columns) and the Mercier criterion  $D_I$  (the third columns) for fixed (the first row) and free (the second row) boundary MHD equilibria with  $\iota_v = 1.48$  in the inward-shifted configuration with  $\gamma_c = 1.254$  and for MHD equilibrium with  $\iota_v = 1.83$  in the inward-shifted configuration with  $\gamma_c = 1.220$  (the third row). Blue, green, yellow and red lines correspond to  $\beta = 1\%$ ,  $2\%$ ,  $3\%$  and  $4\%$ , respectively.

The average magnetic well in the free boundary equilibria becomes deeper and wider than that in the fixed boundary equilibria as  $\beta$  increases, leading to significant improvement of the Mercier criterion in the free boundary equilibria compared with that in the fixed boundary equilibria, where the negative (positive) sign of the Mercier criterion  $D_I$  corresponds to the Mercier stable (unstable) situation. In the inward-shifted LHD configurations, the Mercier unstable region extends in a whole plasma region at low- $\beta$  due to the magnetic hill created by the vacuum magnetic field and moves to the plasma periphery due to the magnetic well formation in the plasma core region by a large Shafranov shift, as  $\beta$  increases. For the fixed boundary MHD equilibria, however, the Mercier criterion is not easy to improve as  $\beta$  increases. In contrast,  $D_I$  is easy to improve for free boundary MHD equilibria. Comparing figure 10 with the first column of figure 8, it is understood that the significant improvement of  $D_I$  mainly comes from the change of the plasma boundary (reduction of poloidally symmetric components) brought about by the free boundary motion of the MHD equilibrium. Although the magnetic well formation in the plasma core region is brought about by a large Shafranov shift even for fixed boundary MHD equilibria, such influences on the Mercier stability do not become effective compared with free boundary equilibrium, because the geometrical change is

not allowed near the plasma boundary. Note that the changes in  $\iota$  and  $D_I$  become significant for  $\beta \gtrsim 2\%$ . Comparing free boundary equilibrium in the inward-shifted configuration with  $\gamma_c = 1.254$  (the second rows) and free boundary equilibrium in the inward-shifted configuration with  $\gamma_c = 1.220$  (the third rows), MHD equilibria in the inward-shifted configuration with  $\gamma_c = 1.220$  are more unstable than those in the inward-shifted configuration with  $\gamma_c = 1.254$  from the aspect of the Mercier criterion, which comes from the fact that the magnitude of the Shafranov shift in MHD equilibria in the inward-shifted configuration with  $\gamma_c = 1.220$  is smaller than that in MHD equilibria in the inward-shifted configuration with  $\gamma_c = 1.254$ , as is understood from the comparison between figures 6 and 7.

## 5.2. Effects of boundary modulation on the global mode analyses in the configuration with $\gamma_c = 1.254$

As understood from the differences of the Mercier criterion between fixed and free boundary MHD equilibria, the influences of the boundary modulation (reduction of the poloidally symmetric components) by the internal current, namely the Pfirsch–Schlüter current, are considered to be significant on the global ideal modes. In order to confirm this expectation, the global mode stability analyses are performed

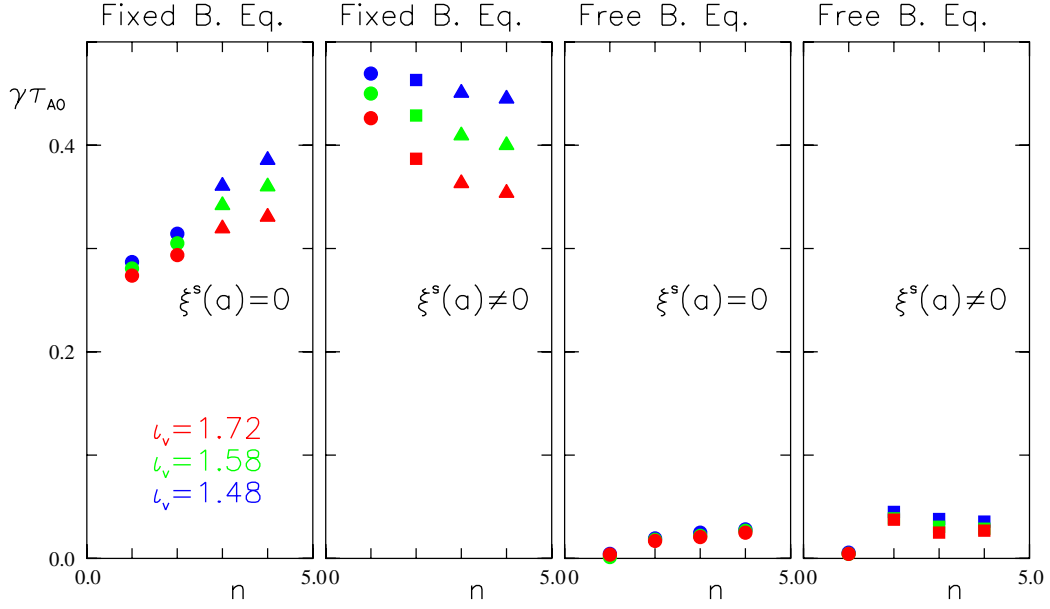


**Figure 11.** Normalized growth rate  $\gamma \tau_{A0}$  versus toroidal mode number  $n$  for MHD equilibria ( $\beta = 3\%$ ) with fixed boundary (the first and the second columns) and with free boundary (the third and the fourth columns). Global mode stability analyses are performed for fixed boundary condition with  $\xi^s(a) = 0$  (the first and the third columns) and for free boundary condition with  $\xi^s(a) \neq 0$  (the second and the fourth columns). Blue, green and red colours correspond to the MHD equilibria with the vacuum rotational transform at the plasma boundary being  $\iota_v = 1.48$ ,  $\iota_v = 1.58$  and  $\iota_v = 1.72$ , respectively. Circles (triangles) denote interchange (tokamak-like ballooning) modes. The squares indicate the ballooning-like structure induced by the free boundary motion with  $\xi^s(a) \neq 0$ .

in the inward-shifted configuration with  $\gamma_c = 1.254$  under the free boundary condition with  $\xi^s \equiv \tilde{\xi} \cdot \nabla s \neq 0$  at the plasma boundary ( $\xi^s(a) \neq 0$ ) or under the fixed boundary condition with  $\xi^s \equiv \tilde{\xi} \cdot \nabla s = 0$  at the plasma boundary ( $\xi^s(a) = 0$ ), using cas3d3 code [14], where  $\tilde{\xi}$  is the displacement vector and  $\xi^s(a)$  indicates the normal (radial) displacement  $\xi^s$  at the plasma–vacuum boundary. The mass density  $\rho_m$  is assumed to be uniform, which is consistent with the experimental observation except that density very near the plasma boundary. Incompressible perturbations are mainly used, in order to simply evaluate the effects of the ion diamagnetic rotation using the eigenvalues obtained by cas3d3. Since the stability of the MHD equilibrium is only determined by the sign of the potential energy  $\delta W_P$ , the MHD equilibrium is stable (unstable) for the perturbations with  $\delta W_P > 0$  ( $\delta W_P < 0$ ) and the kinetic energy is usually evaluated using such a reduced form that the matrix expressing the kinetic energy is diagonalized. However, in the present analyses, the kinetic energy is correctly evaluated using the perpendicular displacement  $\tilde{\xi}_\perp$ , namely,  $\delta W_K = \int (\rho_m/2) |\tilde{\xi}_\perp|^2 d\tau$ , and so the growth rate  $\gamma$  has the correct physics dimension and the magnitude corresponds to the incompressible limit of the compressible perturbation. The growth rate of the incompressible perturbation is two or three times that of the corresponding compressible perturbation [3].

In the case of the three-dimensional equilibria, the linear perturbations couple with equilibrium through both poloidal and toroidal mode couplings. For three-dimensional configurations with  $M$  toroidal field period, there are  $M/2 + 1$  mode families [14]. These mode families are independent in the linear phase and correspond to the toroidal mode number  $n$  of the linear perturbations in axisymmetric configurations. In the present case, there are  $M/2 + 1 = 6$  mode families, namely  $n_f = 0, 1, 2, 3, 4$  and  $5$ . For example,  $n_f = 1$

mode family consists of the toroidal mode numbers with  $n = 1, 9, 11, 19, \dots$ , namely, the linear eigenfunction belonging to  $n_f = 1$  mode family consists of multiple toroidal mode numbers. For a Mercier unstable region, however, the toroidal mode coupling of perturbations inherent to helical systems becomes so weak that the toroidal mode number  $n (\lesssim M)$  can be used as a good quantum number as well as axisymmetric tori, because every magnetic field line at a Mercier unstable rational surface has an unfavourable magnetic curvature on average. Namely, all the magnetic field lines might be considered as equivalent for the perturbations with  $n (\lesssim M)$  from the aspect of the magnetic curvature, so that such perturbations cannot feel the difference of the magnetic curvature in the toroidal direction [19, 20]. In the Mercier unstable MHD equilibria considered here, the toroidal mode number of the perturbations  $n (\lesssim M)$  acts as a good quantum number.

Figure 11 shows the comparison of global mode stability analyses between fixed (the first and the second columns) and free (the third and the fourth columns) boundary MHD equilibria with  $\beta = 3\%$  for three types of MHD equilibria with different plasma–vacuum boundary denoted by  $\iota_v$ . The global mode stability analyses are performed for the fixed boundary condition with  $\xi^s(a) = 0$  (the first and the third columns) and the free boundary condition with  $\xi^s(a) \neq 0$  (the second and the fourth columns), where the growth rates of the most unstable modes normalized by the Alfvén transit time on the magnetic axis  $\gamma \tau_{A0}$  are drawn with respect to the toroidal mode number  $n$ , where  $\tau \equiv \sqrt{\mu_0 \rho_m} / (2\pi t) dV/d\Phi_T$  with the toroidal flux  $\Phi_T$  and the permeability in the vacuum  $\mu_0$ . For typical high- $\beta$  LHD operation parameters with the field strength  $B \sim 0.5$  T and proton density  $n_e \sim 3 \times 10^{19} \text{ m}^{-3}$ ,  $\gamma \tau_{A0} = 0.1$  corresponds to around  $40 \mu\text{s}$ . The most dominant Fourier modes corresponding to figure 11 are summarized in

**Table 5.** The most dominant Fourier modes for fixed ( $\xi^s(a) = 0$ ) and free ( $\xi^s(a) \neq 0$ ) boundary stability analyses in fixed and free boundary equilibria with  $\beta = 3\%$ . The arrow indicates that the most dominant Fourier mode changes according to the plasma–vacuum boundary form  $t_v = 1.48$  to  $t_v = 1.58$ .

Equilibrium	/Stability	Most dominant Fourier mode ( $m, n$ ) for each $n$			
Fixed boundary	$/\xi^s(a) = 0$	(2, 1)	(4, 2)	(5, 3)	(7, 4)
	$/\xi^s(a) \neq 0$	(2, 1)	(3, 2)	(5, 3)	(6, 4) $\rightarrow$ (7, 4)
Free boundary	$/\xi^s(a) = 0$	(1, 1)	(3, 2)	(4, 3)	(6, 4)
	$/\xi^s(a) \neq 0$	(1, 1)	(3, 2)	(4, 3)	(6, 4)

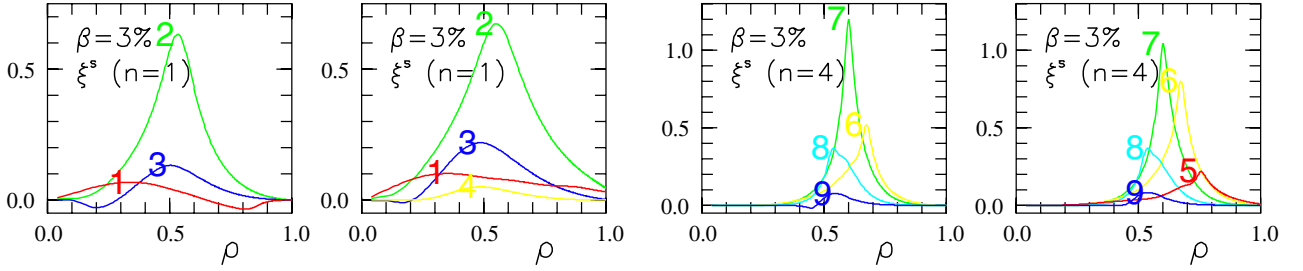


**Figure 12.** Radial profiles of Fourier components of the normal displacement  $\xi^s$  of the eigenfunction for  $n = 1$  (the first and second columns) and for  $n = 4$  (the third and fourth columns) in the fixed boundary MHD equilibrium with  $t_v = 1.72$  for  $\beta = 3\%$ . Eigenfunctions in the first and third (the second and fourth) columns indicate perturbations under the fixed (free) boundary with  $\xi^s(a) = 0$  ( $\xi^s(a) \neq 0$ ). The corresponding growth rates are drawn in the first and the second columns of figure 11. The attached numbers denote the poloidal mode numbers  $m$ .

table 5 for fixed ( $\xi^s(a) = 0$ ) and free ( $\xi^s(a) \neq 0$ ) boundary stability analyses in fixed and free boundary MHD equilibria. Fixed boundary perturbations with  $\xi^s(a) = 0$  in the fixed boundary MHD equilibria (the first column in figure 11) have clear properties of the pressure-driven modes, namely, the growth rates  $\gamma$  become larger as the toroidal mode number  $n$  increases. Moreover, the mode structure changes from the interchange modes denoted by circles ( $n = 1$  and 2) to the ballooning modes indicated by triangles ( $n = 3$  and 4). The radial profiles of the Fourier modes of the normal displacement  $\xi^s$  for  $n = 1$  and 4 modes are shown in the first and the third columns of figure 12.

It might be useful to explain the ballooning modes in the three-dimensional magnetic configurations. Although the three-dimensional magnetic configurations like LHD have a stellarator-like magnetic shear with the opposite sign to that in standard tokamaks, it has been analytically shown that there is a possibility that the local magnetic shear in the stellarator-like (global) magnetic shear region disappears when the Shafranov shift becomes large [19]. In these stellarator-like global magnetic shear region, there are two types of ballooning modes depending on the Mercier stability [20, 21]. One is the tokamak-like ballooning mode with weak toroidal mode coupling, and the other is the ballooning mode with strong toroidal mode coupling inherent to the three-dimensional configurations. The former consists mainly of the Fourier modes with the same toroidal mode number  $n$  as well as the tokamak cases, and the latter consists of the Fourier modes with different toroidal mode numbers. In a Mercier unstable region, both types of ballooning modes become unstable and the ballooning modes with strong toroidal mode coupling inherent to the three-dimensional configurations have larger growth rates than tokamak-like ballooning modes. On the other hand, in the Mercier stable region, only ballooning modes with strong toroidal mode coupling become unstable. Ballooning

modes with strong toroidal mode coupling inherent to the three-dimensional configurations typically have larger poloidal and toroidal mode numbers than tokamak-like ballooning modes ( $m \sim n \gg M$ ). In the present situations, both the most dominant Fourier modes indicated in table 5 and almost all other excited Fourier components have resonant surfaces in the Mercier unstable region, namely, all unstable modes are excited in the Mercier unstable region with a stellarator-like global magnetic shear (see figure 10).

In the fixed boundary MHD equilibria, local mode analyses using the high- $n$  ballooning equation show that high- $n$  ballooning modes are unstable in the Mercier unstable region. Thus, the ballooning modes for  $n = 3$  and 4 under the fixed boundary condition with  $\xi^s(a) = 0$  in the fixed boundary MHD equilibria shown in the first column of figure 11 are pure tokamak-like ballooning modes. The radial profile of Fourier components of the normal displacement  $\xi^s$  of the eigenfunction for  $n = 4$  is shown in the third column of figure 12. Perturbations under the free boundary condition with  $\xi^s(a) \neq 0$  (the second column in figure 11) have completely different toroidal mode number  $n$  dependence from those under the fixed boundary conditions with  $\xi^s = 0$ , namely the growth rates decrease (increase) with respect to the toroidal mode number  $n$  for free (fixed) boundary perturbations. The reason comes from the radial structure of the eigenfunctions.  $n = 1$  and 2 perturbations under the fixed boundary condition are radially global interchange modes with much wider radial widths than tokamak-like ballooning modes with  $n = 3$  and 4, as shown in the first and third columns of figure 12. Thus, the global interchange modes with  $n = 1$  and 2 are more destabilized by the free boundary condition with  $\xi^s(a) \neq 0$  than tokamak-like ballooning modes with  $n = 3$  and 4 [3]. As is understood by comparing the first and the second (the third and the fourth) columns in figure 12, when the free boundary motion is allowed, each Fourier mode has a tendency



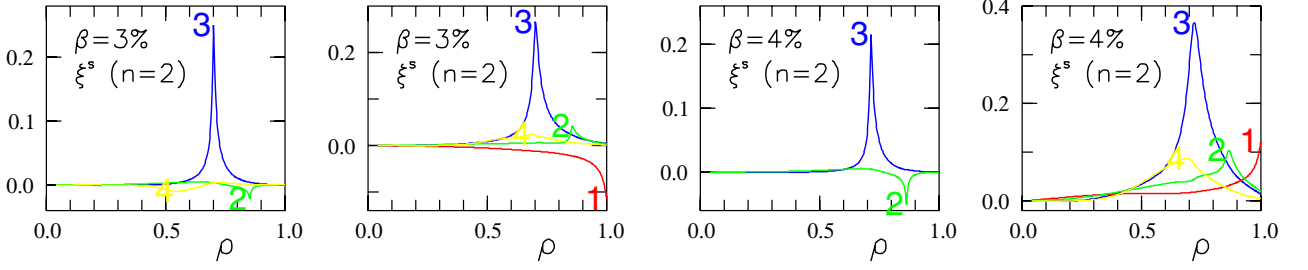


**Figure 13.** Radial profiles of Fourier components of the normal displacement  $\xi^s$  of the eigenfunction in the free boundary MHD equilibrium with  $\iota_v = 1.72$  for  $\beta = 3\%$  (the first and second columns), which correspond to the growth rates with  $n = 2$  in the third and fourth columns of figure 11, and for  $\beta = 4\%$  (the third and fourth columns). Eigenfunctions in the first and third (the second and fourth) columns indicate perturbations under the fixed (free) boundary with  $\xi^s(a) = 0$  ( $\xi^s(a) \neq 0$ ). The attached numbers denote the poloidal mode numbers  $m$ .

to have the same sign or phase outside the torus and the Fourier modes with the rational surfaces near the plasma periphery are additionally excited. These changes by the free boundary motion make the eigenmodes more radially global. The difference of the growth rates between fixed boundary condition with  $\xi^s(a) = 0$  and free boundary condition with  $\xi^s(a) \neq 0$  reduces as  $n$  increases, because higher  $n$  modes have more localized radial structures than lower  $n$  modes.

It is quite clear from figure 11 that free boundary MHD equilibria are significantly stable compared with the corresponding MHD equilibria with the fixed boundary, partially because the Mercier stability  $D_I$  in free boundary equilibria is significantly improved compared with that in the fixed boundary equilibria and partially because the dangerous low- $n$  rational surfaces, especially  $\iota = 1/2$ , disappear in free boundary equilibria (see figure 10). Basic properties of the significant differences are understood by comparing fixed boundary perturbations between fixed and free boundary equilibria (the first and third columns in figure 11). Since the rational surface with  $\iota = 1/2$  existing in fixed boundary MHD equilibria disappears for the free boundary MHD equilibria, most dominant Fourier mode with  $n = 1$  or 2 changes from  $(m, n) = (2, 1)$  or  $(4, 2)$  for fixed boundary equilibria to  $(m, n) = (1, 1)$  or  $(3, 2)$  for free boundary equilibria. As a result, the fairly unstable global low- $n$  interchange modes change into weakly unstable localized interchange modes. More significant stabilization comes from the improvement of the Mercier criterion. Through this improvement, the ballooning unstable equilibria under the fixed boundary condition (the first column in figure 11) become nearly ballooning marginal stable equilibria under the free boundary condition (the third column in figure 11). Indeed, the fixed boundary perturbations for  $n = 3$  and 4 change from the ballooning modes in the fixed boundary equilibria into interchange modes in the free boundary equilibria. This fact that free boundary MHD equilibria are near the marginal stability against high- $n$  ballooning modes will be discussed in more detail later. Thus, ballooning-like free boundary perturbations in the free boundary equilibria (the fourth column in figure 11) are not pure tokamak-like ballooning modes but ballooning-like modes induced by the free boundary motion ( $\xi^s(a) \neq 0$ ) of Fourier components of the interchange modes. Figure 13 shows the change of the eigenfunctions (the radial displacements  $\xi^s$ ) by the stability boundary conditions for free boundary equilibrium with  $\iota_v = 1.72$  and  $\beta = 3\%$  or  $\beta = 4\%$ . Under the fixed boundary condition with  $\xi^s(a) = 0$ , the

eigenfunction has an interchange structure (the first and third columns in figure 13). Even and odd Fourier modes have such opposite signs that each Fourier mode is out of (in) phase in the outboard (inboard) of torus. Thus, the radial displacement  $\xi^s$  has no (some) radial nodes in the inboard (outboard) of the torus, which indicates the characteristics of interchange modes [21]. In contrast, under the free boundary condition with  $\xi^s(a) \neq 0$ , the eigenfunction has a ballooning structure (the second and fourth columns in figure 13). Even and odd Fourier modes have such same signs that each Fourier mode is in (out) of phase in the outboard (inboard) of torus. Thus, the radial displacement  $\xi^s$  has no (some) radial nodes in the outboard (inboard) of the torus, which indicates the characteristics of ballooning modes [21]. This property becomes more clear as  $\beta$  increases, as is understood from figure 13. Since each Fourier mode near the plasma periphery radially extends more and overlaps when the non-vanishing normal displacement  $\xi^s(a)$  is allowed at the plasma boundary, so that when the equilibrium is near the marginally stable state of the ballooning mode, isolated Fourier modes making interchange mode structure under the fixed boundary condition with  $\xi^s = 0$  can become a ballooning-like structure under the free boundary condition with  $\xi^s \neq 0$ . Other interesting property is the excitation of the Fourier mode resonating at the mode rational surface outside the plasma ( $n/m - 2/1$ ), which will be mentioned in detail later.

In order to see how much the equilibrium is stable or unstable against high- $n$  ballooning modes, high- $n$  ballooning stability or  $\iota' - P'$  stability diagram corresponding to  $s - \alpha$  stability diagram in tokamak plasma are evaluated using the method of profile variations, where  $\iota' = dt/d\psi$  and  $P' = dP/d\psi$ , respectively [22]. It has been found out that all the free boundary MHD equilibria with  $\beta = 3\%$  or  $\beta = 4\%$  are in the second stable region or strongly stable in the plasma core region and near the marginally stable states in the plasma periphery against the high- $n$  ballooning modes. Figure 14 shows the example of the  $\iota' - P'$  stability diagrams in the plasma core region (the first column) and in the plasma periphery (the second column) for MHD equilibrium with vacuum boundary of  $\iota_v = 1.48$ . In these analyses, the radial wave number  $\theta_k$  is set 0 and the most dangerous magnetic field line is selected in each flux surface. In figure 14, solid (dotted) lines indicate the marginally stability boundaries for MHD equilibrium with  $\beta = 3\%$  ( $\beta = 4\%$ ). Two rectangles in each graph indicate the location of the original surfaces for two  $\beta$  values, and the location moves along the direction of arrow as  $\beta$  increases.

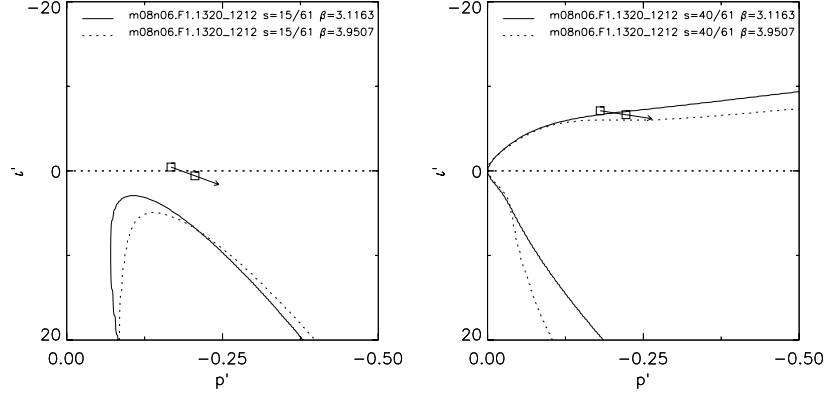


**Figure 14.** Stability diagram of high- $n$  ballooning modes in  $t' - P'$  plane at two flux surfaces in the plasma core ( $\rho \sim 0.29$ , the first column) and in the plasma periphery ( $\rho \sim 0.82$ , the second column) for MHD equilibrium with vacuum boundary of  $t_v = 1.48$ . Note that since  $t$  is negative in these analyses, the vertical axis has an opposite sign to standard usage and  $t'$  is positive (negative) in plasma core (periphery). Solid (dotted) lines indicate the marginally stable lines for  $\beta = 3\%$  ( $\beta = 4\%$ ). Rectangles denote the location of the original flux surfaces, and arrows show the direction of the change of the location with increasing  $\beta$ .

It is quite clear that the plasma core region is strongly stable against high- $n$  ballooning modes, and that these properties do not change as  $\beta$  increases, namely, the core region has a tendency to move to the second stability region as  $\beta$  increases. In contrast, it is also clear that in the plasma periphery, the MHD equilibrium exists around the marginally stable state against the high- $n$  ballooning modes. This tendency does not change in the range of  $\beta$  value used in stability analyses. Moreover, it might be expected that the MHD equilibria with higher  $\beta$  values still exist near the marginally stable states against high- $n$  ballooning modes near the plasma periphery.

One of the characteristics of the stability analyses for free boundary MHD equilibria is that interchange mode with an externally resonant Fourier component, namely,  $(m, n) = (1, 2)$  is excited as shown in the second and fourth columns in figure 13, where a larger plasma boundary with  $t_v = 1.72$  is chosen. This component of Fourier mode is usually observed in the high- $\beta$  plasma in the inward-shifted configuration with  $\gamma_c = 1.220$ , as is shown in figure 2 and table 2 [10]. In these perturbations given in the second and the fourth columns of figure 13,  $(m, n) = (1, 2)$  mode may be dominantly observed experimentally, because the magnitude of the magnetic perturbation of each Fourier mode in the vacuum region is determined by the magnitude of the normal displacement at the plasma boundary  $\xi^s(a)$ , and the magnetic probes detect the vacuum magnetic perturbations. Moreover, experimentally observed Fourier mode:  $(m, n) = (2, 3)$  [11] is excited as the second most unstable mode as shown in figure 15. Experimentally observed Fourier modes, however, appear only as externally resonating Fourier components in these stability analyses. For example, the mode rational flux surface with  $t = 3/2$  exists inside the plasma for the MHD equilibria with the vacuum boundary  $t_v = 1.72$ . However, the Fourier components with  $(m, n) = (2, 3)$  does not have such a large amplitude at the plasma boundary that the most dominant Fourier mode of the vacuum magnetic perturbation becomes  $(m, n) = (2, 3)$ , the reason of which might be considered to be due to the pressure and density profiles near the plasma periphery. The pressure profile near the plasma periphery might strongly affect the excitation of the Fourier modes with the mode rational surfaces there through the Mercier criterion

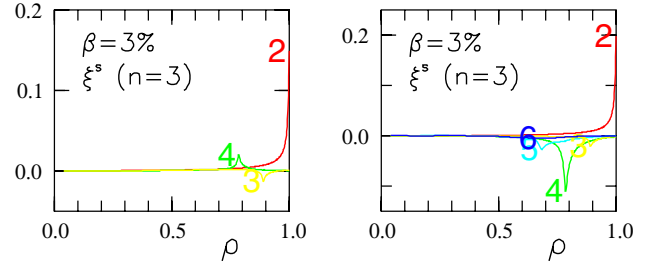


**Figure 15.** Radial profiles of Fourier components of the normal displacement  $\xi^s$  of the eigenfunction with an externally resonant Fourier component:  $(m, n) = (2, 3)$  for the free boundary MHD equilibrium with  $t_v = 1.48$  and  $\beta = 3\%$ . The first column corresponds to the second most unstable mode for  $n = 3$  for uniform density, i.e.  $\rho_m = \text{const}$ . This mode becomes the most unstable mode for  $n = 3$ , shown in the second column, for non-uniform density with  $\rho_m = \rho_0(1 - s^{10}/2)$ . The attached numbers denote the poloidal mode numbers  $m$ .

$D_I$ . When the gradient of the pressure profile is fairly weak or  $dP/ds \sim 0$  near the plasma boundary, the region near the plasma boundary becomes Mercier stable ( $D_I < 0$ ). Thus, ideal interchange modes with the resonant rational surfaces near the plasma boundary with  $D_I < 0$  become stable. On the other hand, the effects of the density profile are understood from the comparison between the first and second columns in figure 15, where uniform density (the first column) and non-uniform density (the second column) are used. Since the mass density in the place where the perturbations are localized mainly contributes to determine the magnitude of the growth rates and the structure of eigenfunctions, the density profile near the plasma boundary significantly influences the growth rate of the perturbations with Fourier modes resonating at the external rational surfaces.

The  $\beta$ -dependences of the growth rates of the fixed boundary perturbations with  $\xi^s(a) = 0$  are shown in figure 16 for 4 mode families, in three free boundary MHD equilibria with different boundary. As is understood from the discussions in figures 11 and 14, MHD equilibria under the free boundary condition are ballooning stable in the core region and near ballooning marginally stable in the peripheral region, so that all

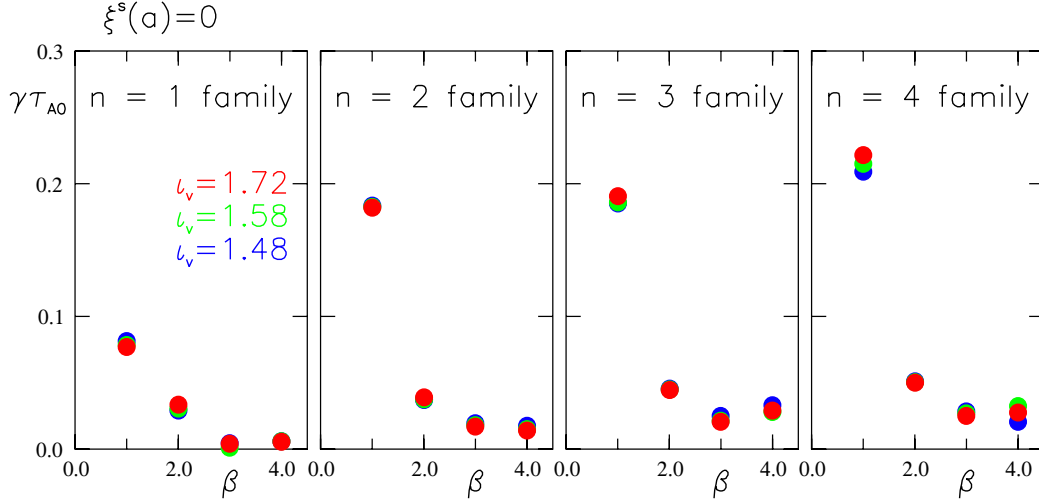


**Figure 16.**  $\beta$ -dependences of the normalized growth rates  $\gamma\tau_{A0}$  for 4 mode families under the fixed boundary stability condition with  $\xi^s(a) = 0$ . Blue, green and red symbols correspond to free boundary MHD equilibria with  $\iota_v = 1.48$ ,  $\iota_v = 1.58$  and  $\iota_v = 1.72$ , respectively. Only interchange modes are unstable.

**Table 6.**  $\beta$ -dependence of the most dominant Fourier modes in free boundary equilibria with different vacuum boundary. The arrow indicates that the most dominant Fourier mode changes according to the plasma–vacuum boundary from  $\iota_v = 1.48$  to  $\iota_v = 1.58$ . Most dominant Fourier mode for each toroidal mode number  $n$  does not change between fixed boundary with  $\xi^s(a) = 0$  and free boundary with  $\xi^s(a) \neq 0$  stability conditions.

Equilibrium	Most dominant Fourier mode $(m, n)$ for each $n$			
$\beta = 1\%$	(2, 1)	(5, 2)	(8, 3)	(11, 4)
$\beta = 2\%$	(2, 1)	(4, 2)	(5, 3) $\rightarrow$ (6, 3)	(7, 4)
$\beta = 3\%$	(1, 1)	(3, 2)	(4, 3)	(6, 4)
$\beta = 4\%$	(1, 1)	(3, 2)	(4, 3)	(6, 4) $\rightarrow$ (5, 4)

the perturbations under the fixed boundary stability condition are interchange modes.

As is understood from table 6, where the most dominant Fourier mode for each  $n$  is indicated for various  $\beta$ , in low- $\beta$  free boundary equilibria, fairly radially global interchange modes with the resonant surfaces in the plasma core region become unstable. As  $\beta$  increases, the Mercier criterion much improves from the core to the peripheral plasma region and the dangerous low- $n$  rational surfaces disappear, so that the unstable region moves from the plasma core into plasma periphery (see figure 10) and the growth rates are significantly reduced independent of the choice of plasma–vacuum boundary. Note that even in high- $\beta$  ( $\beta = 4\%$ ), free boundary MHD equilibria are nearly ballooning marginally stable and the growth rates do not increase so much as  $\beta$  increases as shown in figure 16.

The  $\beta$ -dependences of the growth rates of the free boundary perturbations  $\xi^s(a) \neq 0$  are shown in figure 17 for 4 mode families, in three free boundary MHD equilibria with different boundaries. For  $\beta < 3\%$ , the behaviour of the growth rates of free boundary perturbations with respect to  $\beta$  value are similar to those of the fixed boundary perturbations. All the most unstable modes are interchange modes, and so this  $\beta$  range is named as the interchange regime. In the interchange regime, the normalized growth rates  $\gamma\tau_{A0}$  decrease as  $\beta$  increases independent of the plasma vacuum boundary

reflecting the change of the rotational transform  $\iota$  and the improvement of the Mercier criterion  $D_I$  in figure 10.

Around or above  $\beta \simeq 3\%$ , eigenmodes change into free boundary induced ballooning modes except for  $n_f = 1$  mode family, and so this range of  $\beta$  is named as the ballooning regime. In the ballooning regime, the normalized growth rates  $\gamma\tau_{A0}$  increase as  $\beta$  increases independent of the plasma vacuum boundary. In the interchange regime, the growth rates do not depend on the plasma boundary, however, in the ballooning regime, larger plasmas have more stable modes with smaller growth rates. As mentioned, high- $n$  ballooning analyses show that the MHD equilibrium under the free boundary condition is strongly stable in the core region and near the marginally stable state in the plasma periphery, moreover, ballooning-like modes indicated by the square symbols in figure 11 appear as interchange modes under the fixed boundary stability analyses as shown in figure 16. Thus, the ballooning properties of the unstable modes under the free boundary stability analyses for free boundary MHD equilibria with  $\beta \geq 3\%$  is considered to come from the radial extension and overlapping of the envelope of each Fourier mode allowed by the free boundary condition:  $\xi^s(a) \neq 0$ .

The stabilizing effects of the ion diamagnetic rotation are considered as follows, where ions are assumed to be protons. For the incompressible perturbations, the linearized equation of motion including the ion diamagnetic frequency is expressed as

$$\rho_m[-\omega^2 \vec{\xi}_\perp - i\omega \vec{v}_{Di} \cdot \nabla \vec{\xi}_\perp] = \vec{F}(\vec{\xi}_\perp), \quad \vec{v}_{Di} = \frac{\vec{B} \times \nabla P_i}{en_i B^2}, \quad (4)$$

where  $\vec{v}_{Di}$  is the ion diamagnetic drift velocity with ion density  $n_i$  and pressure  $P_i$ , and  $\vec{F}(\vec{\xi}_\perp)$  is the standard self-adjoint ideal MHD force operator. The correction by the ion diamagnetic frequency in currentless MHD equilibria is read as

$$\begin{aligned} \vec{v}_{Di} \cdot \nabla \vec{\xi}_\perp &= \frac{1}{en_i} \frac{dP_i}{d\psi} \sum_{mn} im \vec{\xi}_{\perp mn} = \sum_{mn} i\omega_{*i} m \vec{\xi}_{\perp mn}, \quad \omega_{*i} \\ &\equiv \frac{1}{en_i} \frac{dP_i}{d\psi} m \end{aligned} \quad (5)$$

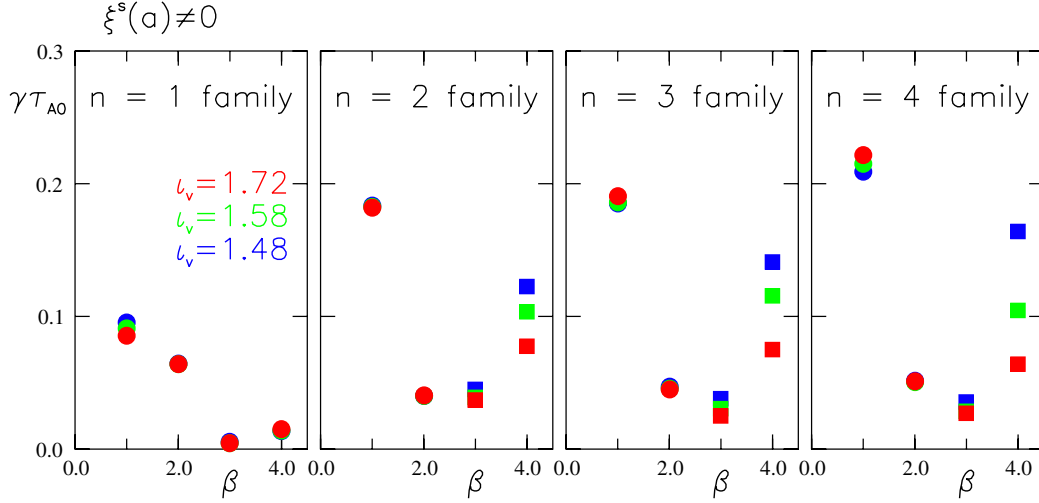


**Figure 17.**  $\beta$ -dependences of the growth rates for 4 mode families under the free boundary stability condition with  $\xi^s(a) \neq 0$ . Blue, green and red symbols correspond to free boundary MHD equilibria with  $t_v = 1.48$ ,  $t_v = 1.58$  and  $t_v = 1.72$ , respectively. Circles (squares) indicate interchange (free boundary induced ballooning) modes.

where  $\vec{\xi}_\perp$  is Fourier decomposed, and  $\omega_{*im}$  is the ion diamagnetic frequency for the Fourier mode with the poloidal mode number  $m$ . Substituting equation (5) into equation (4), we obtain

$$\rho_m \left[ -\omega^2 \vec{\xi}_\perp + \sum_{mn} \omega \omega_{*im} \vec{\xi}_{\perp mn} \right] = \vec{F}(\vec{\xi}_\perp). \quad (6)$$

In the present analyses, the pressure profile is  $P(s) = P(0)(1-s)(1-s^9)$  and uniform density ( $n_e = \text{const}$ ) is assumed. When  $P_i = P/2$  or  $T_e = T_i$  is assumed, the ion diamagnetic frequency  $\omega_{*im}$  given by equation (5) is almost constant except for near the plasma boundary. Thus, for interchange modes with a single dominant Fourier mode ( $m, n$ ), in equation (6)  $\sum_{mn} \omega \omega_{*im} \vec{\xi}_{\perp mn} \sim \omega \omega_{*im} \vec{\xi}_\perp$ , so that the integration of equation (6) multiplied  $\vec{\xi}_\perp^*$  leads to

$$\omega(\omega - \omega_{*i}) = \lambda, \quad \omega_{*i} = \omega_{*im}, \quad (7)$$

where  $\lambda$  is the eigenvalue obtained by the cas3d3 for incompressible perturbations. Although equation (7) is only applicable to the special cases with both (1) almost uniform ion diamagnetic frequency  $\omega_{*im}$ , which is satisfied in the present analyses and (2) interchange modes with a single dominant Fourier mode, which is satisfied for interchange modes in low- $\beta$  ( $\lesssim 2\%$ ) equilibria, the stabilizing effects by the ion diamagnetic rotation are recognized. Note that if equation (7) is almost exact for some perturbations, then the perturbations are unstable for the condition  $\sqrt{-\lambda} > |\omega_{*i}|/2$  is satisfied and the growth rates are modified by the ion diamagnetic frequency as  $\gamma = \sqrt{-\lambda - \omega_{*i}^2}/4$ . Thus, as a rough estimation, the ion diamagnetic frequency  $\omega_{*i}$  for the most dominant Fourier modes is evaluated against the growth rates. The growth rates  $\gamma$  are in the range of  $\omega_{*i}$  for typical experimental parameters with  $B \sim 0.5$  T and  $n_e \sim 3 \times 10^{19} \text{ m}^{-3}$ , except for all equilibria with  $\beta \sim 1\%$  and for smaller size equilibria ( $t_v = 1.48$ ) with  $\beta = 4\%$ , so that instabilities in the free boundary MHD equilibria with larger plasma size might be considered to be harmless for  $\beta > 1\%$ . Also, it might be useful to note that

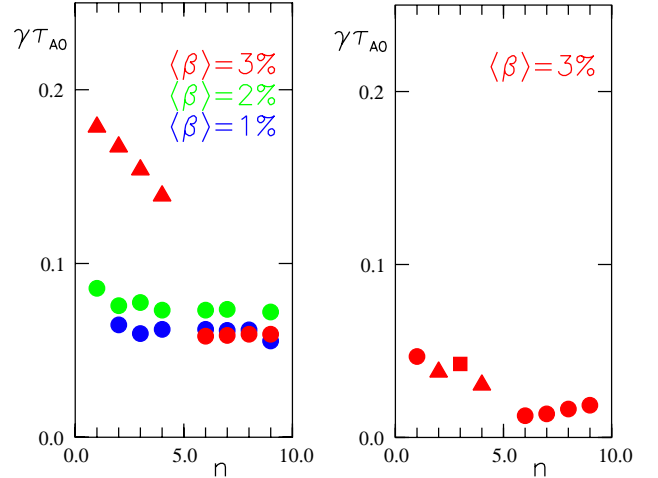


**Figure 18.** The normalized growth rates  $\gamma\tau_{A0}$  for compressible perturbations versus the toroidal mode number  $n$  in MHD equilibria with the original (the first column) and modulated (the second column) fixed boundaries. Circles (triangles) indicate the interchange (ballooning or ballooning-like) modes. Rectangles in the MHD equilibrium with modulated fixed boundary mean the perturbation with externally resonant Fourier component experimentally observed like the one in figure 15. Blue, green and red symbols correspond to  $\beta = 1\%$ ,  $\beta = 2\%$  and  $\beta = 3\%$ , respectively.

the growth rates of compressible perturbations are one-half or one-third of those of incompressible perturbations [3].

Finally, in order to confirm that reduction of the poloidally symmetric components leads to the significant stabilizing effects, the stability analyses are performed for MHD equilibria under such a fixed boundary that the only poloidally symmetric components are eliminated from the original boundary with  $t_v = 1.48$ . It is understood from this modulation of the plasma boundary that (1) the similar improvement of the Mercier criterion is obtained, leading to the significant reduction of the growth rates as shown in figure 18 where the normalized growth rates  $\gamma\tau_{A0}$  for compressible perturbations versus the toroidal mode number  $n$  are drawn for the MHD equilibria with



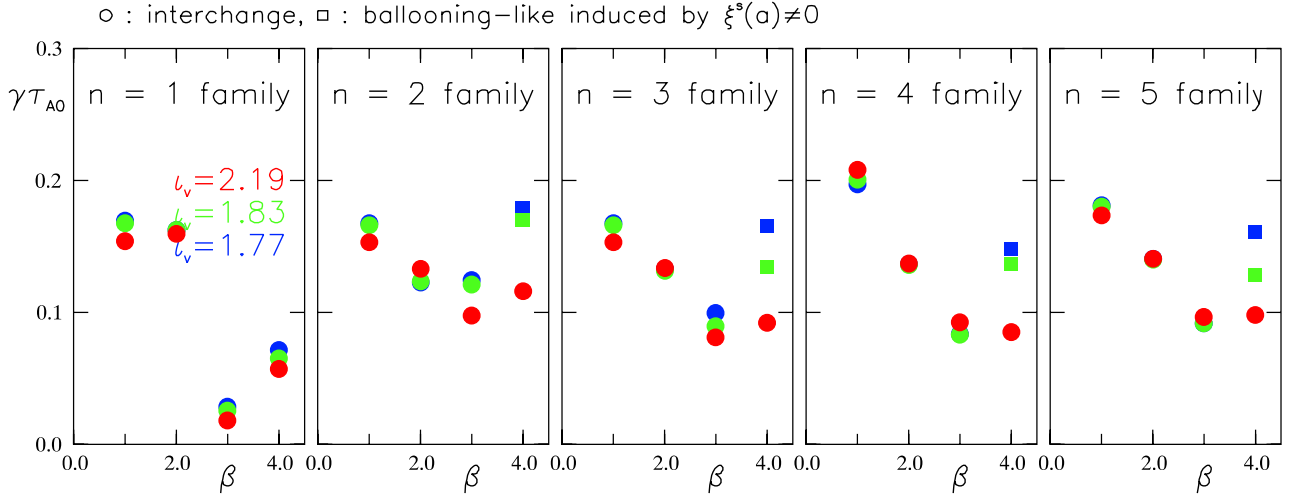


**Figure 19.**  $\beta$ -dependences of the normalized growth rates  $\gamma\tau_{A0}$  for 5 mode families under the free boundary stability condition with  $\xi^s(a) \neq 0$ , where incompressible perturbations are used. Blue, green and red symbols correspond to free boundary MHD equilibria with  $t_v = 1.77$ ,  $t_v = 1.83$  and  $t_v = 2.19$ , respectively. Circles (squares) indicate interchange (free boundary induced ballooning) modes.

**Table 7.**  $\beta$ -dependence of the most dominant Fourier modes in free boundary equilibria with different vacuum boundary for inward-shifted configuration with  $\gamma = 1.220$ . The arrow indicates that the most dominant Fourier mode changes according to the plasma–vacuum boundary from  $t_v = 1.83$  to  $t_v = 2.19$ .

Equilibrium	Most dominant Fourier mode $(m, n)$ for each $n$				
$\beta = 1\%$	(2, 1)	(4, 2)	(6, 3)	(9, 4)	(11, 5)
$\beta = 2\%$	(2, 1)	(4, 2)	(5, 3) $\rightarrow$ (6, 3)	(7, 4)	(9, 5)
$\beta = 3\%$	(1, 1)	(3, 2)	(4, 3)	(6, 4)	(7, 5)
$\beta = 4\%$	(1, 1)	(3, 2)	(4, 3)	(5, 4)	(6, 5) $\rightarrow$ (7, 5)

original (the first column) and modulated (the second column) fixed boundary and (2) the similar perturbations, which have the externally resonant Fourier component observed in the experiments, to that in figure 11 are excited.

### 5.3. Effects of boundary modulation on the global mode analyses in the configuration with $\gamma = 1.220$

Stabilizing effects of boundary modulation are investigated in the inward-shifted configuration with  $\gamma_c = 1.220$ . Figure 19 shows the  $\beta$ -dependence of the normalized growth rates  $\gamma\tau_{A0}$  for 5 mode families under the free boundary stability condition with  $\xi^s(a) \neq 0$ , where incompressible perturbations are used as well as in the configuration with  $\gamma_c = 1.254$ . As well as in the configuration with  $\gamma_c = 1.254$ , stabilizing effects brought by the boundary modulation, namely the whole plasma outward shift are clear up to  $\beta = 3\%$ , although the growth rates are larger than those in the configuration with  $\gamma_c = 1.254$ . This difference of the growth rates comes from the fact that the improvement of Mercier criterion in the configuration with  $\gamma_c = 1.220$  is weak compared with that in the configuration with  $\gamma_c = 1.254$  as is seen in figure 10.

Most unstable Fourier modes are summarized in table 7. As well as the configuration with  $\gamma_c = 1.254$ , dangerous global interchange modes with  $n/m = 1/2$  disappear as  $\beta$  increases.

Although the stabilizing effects due to boundary modulation are clear, the growth rates of the incompressible perturbations are so high that the diamagnetic stabilizing effects might not be enough for those incompressible

perturbations to become harmless. In order to see realistic growth rates, the ideal MHD stability analyses are performed for compressible perturbations. The comparison of the growth rates between incompressible and compressible perturbations are shown in figure 20 for the free boundary MHD equilibria with  $t_v = 1.83$ . The magnitude of the growth rates is less than  $0.05/\tau_{A0}$ , so that it is expected that some kinetic effects like diamagnetic rotation make those modes harmless, which might be consistent with the experimental observation without confinement degradation and stability  $\beta$  limit, as well as in the inward-shifted LHD configuration with  $\gamma_c = 1.254$ .

Finally, effects of the steep pressure gradient at the plasma boundary are investigated by changing the pressure profile from  $P(s) = P(0)(1-s)(1-s^9)$  to  $P(s) = P(0)(1-s)$  in the MHD equilibria with  $t_v = 2.19$  as shown in figure 21. Although the growth is underestimated, since the surface terms of the potential is not included in cas3d3, the modes with externally resonating Fourier component  $n/m = 5/2$  are destabilized as the most unstable modes. This result indicates that the steep pressure gradient near the plasma boundary has a possibility of exciting the experimentally observed modes near the plasma boundary. As well as the cases in the inward-shifted LHD configurations with  $\gamma_c = 1.254$ , experimentally observed Fourier modes with the resonant rational surfaces beyond the vacuum LCFS are destabilized only as the externally resonant Fourier component, because the region near the plasma boundary is Mercier stable ( $D_I < 0$ ) due to the weak pressure gradient ( $dP/ds \sim 0$ ).

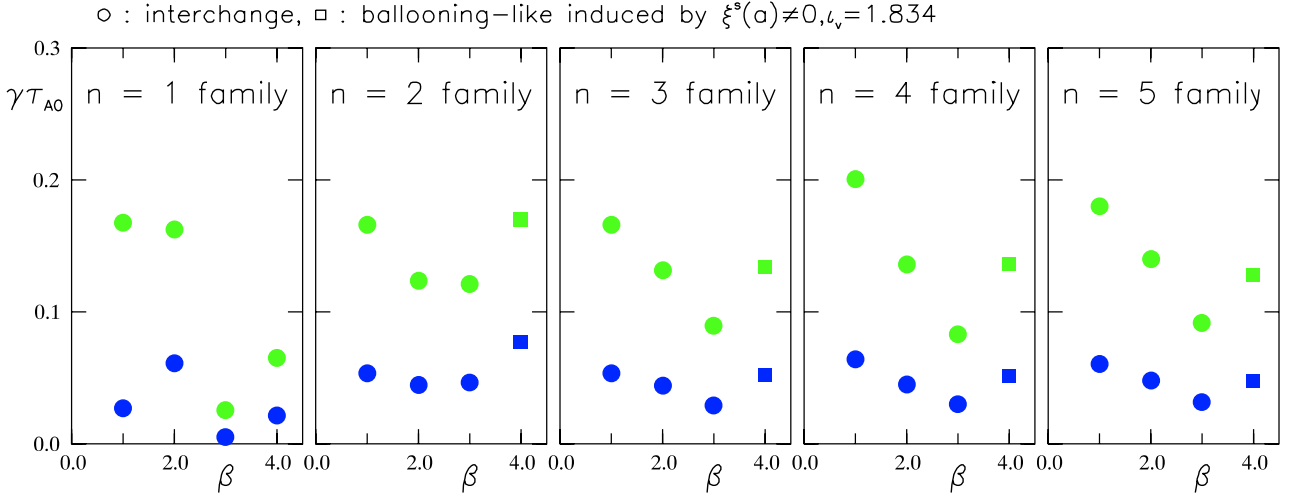


**Figure 20.**  $\beta$ -dependences of the normalized growth rates  $\gamma\tau_{A0}$  for 5 mode families under the free boundary stability condition with  $\xi^s(a) \neq 0$  for incompressible (green) and compressible (blue) perturbations in the free boundary MHD equilibria with  $\nu = 1.83$ . Circles (squares) indicate interchange (free boundary induced ballooning) modes.

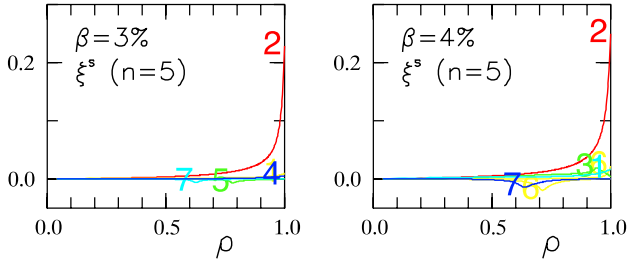


**Figure 21.** Radial profiles of Fourier components of the normal displacement  $\xi^s$  of the eigenfunction with an externally resonant Fourier component:  $(m, n) = (2, 5)$  in the free boundary MHD equilibrium with  $\nu = 2.19$  for  $\beta = 3\%$  (left column) and for  $\beta = 4\%$  (right column). In these calculations, pressure profile is changed from  $P(s) = P(0)(1-s)(1-s^9)$  to  $P(s) = P(0)(1-s)$ , so that these modes with an external resonant component become the most unstable modes in  $n_f = 5$  mode family. The attached numbers denote the poloidal mode numbers  $m$ .

## 6. Summary and discussions

It is well known that a boundary shaping has significant effects on MHD stability and single particle confinements [12]. Thus, such a boundary shaping is mainly done by controlling an external coil current path for designing the devices, however, there is a case in experiments that a large internal plasma current, namely a large Pfirsch–Schlüter current induces additional modulation of the plasma–vacuum boundary as synergetic effects together with the transport in the region with stochastic magnetic field, even if the external coil current condition is fixed. In order to examine effects of the boundary modulations on MHD equilibrium and stability, high- $\beta$  plasmas allowing a large Shafranov shift are considered in the inward-shifted LHD configurations, for which the previous theoretical MHD stability analyses based on the fixed boundary MHD equilibria indicated strong MHD instabilities compared with experimental results [3].

In the case of LHD high- $\beta$  experiments, it is quite natural to consider the boundary modulation realized by the

free boundary MHD equilibrium, because there are standard experimental observations that (1) the electron temperature gradient extends beyond the vacuum LCFS [7], (2) the electron density profile is significantly hollow and extends beyond the vacuum LCFS [8], and (3) from the low- $\beta$  or with increasing  $\beta$ , magnetic perturbations with the resonant rational surfaces near or beyond the vacuum LCFS are observed by the magnetic probes [9–11]. Therefore, to consider the boundary modulation appearing as the plasma outward-shift beyond the vacuum LCFS, together with the experimentally observed net toroidal current condition (currentless condition) and pressure profile (a broad pressure profile with steep gradient near the plasma boundary) leads to the removal of the discrepancy on the MHD equilibria between experimentally obtained and theoretically used. Since such a boundary modulation or plasma outward-shift beyond the vacuum LCFS is brought about by the simultaneous synergetic effects between the MHD equilibrium Pfirsch–Schlüter current due to the pressure gradient, leading to changes in the magnetic field, and the transport in the region with stochastic magnetic field lines, leading to changes in the temperature and the density, the concept of the averaged flux surfaces is introduced in the region with stochastic magnetic field lines, which are defined as the confinement region with a long connection length compared with the parallel mean free path, a definite rotational transform and a small electron thermal conductivity, in order to realize the confinement region in the stochastic region.

It has been shown for the inward-shifted LHD configurations that the boundary modulation has significant stabilizing properties for ideal pressure-driven modes through the improvement of the Mercier criterion and elimination of the dangerous low- $n$  rational surfaces, leading to the partial removal of the discrepancy on MHD stability between experimental results and theoretical consideration. The most significant differences between fixed boundary equilibria without boundary modulation and free boundary equilibria with boundary modulation are that (1) a monotonic increase in the growth rate with  $\beta$  value in the fixed boundary equilibria

disappears in the free boundary equilibria and that (2) high- $n$  ballooning unstable equilibria under the fixed boundary condition change into high- $n$  ballooning marginally stable equilibria under the free boundary condition. One other interesting point is the excitation of the free boundary-induced ballooning modes.

The correspondence between experimentally observed magnetic signals and theoretically obtained unstable modes is not so clear for the modes resonating near the plasma edge even if the experimentally measurable range of the Fourier modes is taken into account. This difference will be analysed in detail taking account of the vacuum magnetic perturbations due to the unstable modes and pressure profiles with more steep gradient near the plasma boundary, and the resistive interchange modes.

In order to create more consistent MHD equilibria between experiment and theory, the transport process in the stochastic magnetic field region is introduced into the MHD equilibrium calculations by modifying HINT or HINT2 algorithm, by which the concept of the averaged flux surfaces will be replaced by a more realistic concept.

## Acknowledgments

The author (N.N.) greatly acknowledges Dr K.Y. Watanabe and Dr S. Sakakibara for their quite fruitful discussions and presenting the Fourier decomposed magnetic signal of the MHD perturbations observed by the magnetic probes.

## References

- [1] Motojima O. *et al* 2003 *Nucl. Fusion* **43** 1674
- [2] Watanabe K.Y. *et al* 2004 *Proc. 20th Int. Conf. on Fusion Energy 2004 (Vilamoura, 2004)* (Vienna: IAEA) CD-ROM file EX/3-3 and <http://www-naweb.iaea.org/naweb/physics/fec/fec2004/datasets/index.html>
- [3] Nakajima N. *et al* 2005 *J. Plasma Fusion Res. Ser.* **6** 45
- [4] Ichiguchi K. *et al* 2003 *Nucl. Fusion* **43** 1101
- [5] Ichiguchi K. *et al* 1993 *Nucl. Fusion* **33** 481
- [6] Ichiguchi K., Nakajima N. and Gardner H. J 1996 *Nucl. Fusion* **36** 1157
- [7] Morisaki T. *et al* 2003 *J. Nucl. Mater.* **313–316** 548
- [8] Tanaka K. *et al* 2004 *Proc. 20th Int. Conf. on Fusion Energy 2004 (Vilamoura, 2004)* (Vienna: IAEA) CD-ROM file EX/P6-28 and <http://www-naweb.iaea.org/naweb/physics/fec/fec2004/datasets/index.html>
- [9] Sakakibara S. 2005 NIFS, private communication
- [10] Sakakibara S. *et al* 2004 *Proc. 31st EPS Conf. on Plasma Physics (London, 2004)* O4-01
- [11] Sakakibara S. *et al* 2002 *Plasma Phys. Control. Fusion* **44** A217
- [12] Nührenberg J. and Zille R. 1986 *Phys. Lett. A* **114** 129
- [13] Hirshman S.P. 1983 *Phys. Fluids* **26** 3553
- [14] Nührenberg C 1999 *Phys. Plasmas* **6** 137
- [15] Hayashi T. *et al* 1994 *Phys. Plasmas* **1** 3262
- [16] Harafuji K. *et al* 1989 *J. Comput. Phys.* **81** 169
- [17] Strumberger E. 1997 *Nucl. Fusion* **37** 19
- [18] Koniges A.E. *et al* *Nucl. Fusion* **43** 107
- [19] Nakajima N. 1996 *Phys. Plasmas* **3** 4545
- [20] Nakajima N. 1996 *Phys. Plasmas* **3** 4556
- [21] Chen J., Nakajima N. and Okamoto M. 1999 *Phys. Plasmas* **6** 1562
- [22] Hegna C.C. and Nakajima N. 1998 *Phys. Plasmas* **5** 1336